mathematics

MDPI

Article

Analytical and Computational Approaches for Bi-Stable Reaction and p-Laplacian Diffusion Flame Dynamics in Porous Media

Saeed ur Rahman [1] and José Luis Díaz Palencia [2,3,*]

[1] Department of Mathematics, COMSATS University Islamabad, Abbottabad Campus, Abbottabad 22060, Pakistan; saeed@cuiatd.edu.pk
[2] Department of Education, Universidad a Distancia de Madrid, 28400 Madrid, Spain
[3] Department of Information Technology, Escuela Politécnica Superior, Universidad San Pablo-CEU, CEU Universities, Campus Monteprincipe, Boadilla del Monte, 28668 Madrid, Spain
* Correspondence: joseluis.diaz.p@udima.es or jose.diazpalencia@ceu.es

Abstract: In this paper, we present a mathematical approach for studying the changes in pressure and temperature variables in flames. This conception extends beyond the traditional second-order Laplacian diffusion model by considering the p-Laplacian operator and a bi-stable reaction term, thereby providing a more generalized framework for flame diffusion analysis. Given the structure of our equations, we provide the boundedness and uniqueness of the solutions in a weak sense from both analytical and numerical approaches. We further reformulate the governing equations in the context of traveling wave solutions, applying singular geometric perturbation theory to derive the analytical expressions of these profiles. This theoretical development is complemented by numerical assessments, which not only validate our theoretical predictions, but also optimize the traveling wave speed to minimize the error between numerical and analytical solutions. Additionally, we explore self-similar structured solutions. The paper then concludes with a perspective on future research, with emphasis being placed on the need for experimental validation in laboratory settings. Such empirical studies could test the robustness of our model and allow for refinement based on actual measurements, thereby broadening the applicability and accuracy of our findings in practical scenarios.

Keywords: flame propagation; bi-stable nonlinearity; p-Laplacian; traveling wave; geometric perturbation theory; self-similarity

MSC: 35Q35; 35B65; 76D05

Citation: Rahman, S.u.; Díaz Palencia, J.L. Analytical and Computational Approaches for Bi-Stable Reaction and p-Laplacian Diffusion Flame Dynamics in Porous Media. *Mathematics* **2024**, *12*, 216. https://doi.org/10.3390/math12020216

Academic Editor: Sergey Ershkov

Received: 13 December 2023
Revised: 3 January 2024
Accepted: 7 January 2024
Published: 9 January 2024

1. Introduction

We depart from a known model based on a classical parabolic operator and a kind of nonlinear reaction term that has been discussed in [1–3], and which is generally expressed as follows:

$$\frac{\partial \tilde{u}}{\partial t} = \frac{\partial^2 \tilde{u}}{\partial y^2} + G(\tilde{u}, \tilde{v}), \tag{1}$$

$$\frac{\partial \tilde{v}}{\partial t} = \frac{\partial^2 \tilde{v}}{\partial y^2} + G(\tilde{u}, \tilde{v}), \tag{2}$$

where $y \in \mathbb{R}$, $t \in (0, T]$, $\tilde{u} \in \mathbb{R}$, $\tilde{v} \in \mathbb{R}$, and $G(\tilde{u}, \tilde{v})$ are continuously differentiable functions. In our case, the function $G(\tilde{u}, \tilde{v})$ is required to satisfy the following fundamental properties (and this also represents a new approach compared to that in [1–3]):

(a) $G(0,0) = G(1,1) = 0$;
(b) $\frac{\partial G}{\partial \tilde{u}}(0,0) < 0$, $\frac{\partial G}{\partial \tilde{v}}(0,0) < 0$, $\frac{\partial G}{\partial u}(1,1) < 0$ and $\frac{\partial G}{\partial v}(1,1) < 0$;
(c) There exists $\mu \in (0,1)$ such that for $\tilde{v} \in (0, \mu)$, then $G(\tilde{u}, \tilde{v}) < 0$ and for $\tilde{v} \in (\mu, 1)$, then $G(\tilde{u}, \tilde{v}) > 0$;

(d) $\int_0^1 \int_0^1 G(\tilde{u}, \tilde{v}) du dv > 0$.

A typical nonlinear example satisfying the above assumptions is

$$G(\tilde{u}, \tilde{v}) = \left(1 - \tilde{v}\right)\left(\tilde{v} - \mu\right)\left(h\tilde{u} + \left(1 - h\right)\tilde{v}\right). \tag{3}$$

This kind of bi-stable nonlinearity has been employed for modeling in other applications like population dynamics and fluid modeling. In the postulated nonlinearity, the first two terms represent cases of critical points when $\tilde{v}$ is equal to either 1 or μ, and the last term refer to critical points when $\tilde{u}$ depends on $\tilde{v}$. For example, if the function $\tilde{v}$ refers to a physical variable in a flame (temperature or pressure), this can evolve between the critical points introduced by the bi-stable term. The flame may also evolve from one of the critical points to a relaxed configuration in which the solutions tend toward zero. In any of the cases, we may explore the connections between critical points. In addition, we should mention that the term $\left(h\tilde{u} + \left(1 - h\right)\tilde{v}\right)$ is well known in the combustion theory of flames, and it will be further described afterward.

Equations (1) and (2) represent the classical parabolic model of interacting and spreading particles, and they have been mostly used in physics (shock waves), in biology (the propagation of nerve pulses, population dynamics, etc.), or in chemistry for flame propagation, combustion, and chemical reactions (see [4–10] for additional insights).

As a first important work in this regard, we should mention that Fisher [11] suggested Equation (1) with a slightly different nonlinearity (specifically considering $h = 0$ in Equation (3)) when he was dealing with genetic interactions in population dynamics. Later on, Aronson and Weinberger [12] also worked on genetic modeling, and they introduced new terminology. In particular, if any given nonlinearity term satisfies the previously stated conditions from (a) to (d), it is referred as heterozygote inferior nonlinearity. Kanel [13] considered a one-dimensional bi-stable case reaction, and they used the traveling waves theory to obtain the existence of a solution when the speed of a wave is positive. In addition, Roussier [14] studied a bi-stable nonlinearity to obtain the asymptotic behavior of solutions to (1) by using spherically symmetric traveling wave profiles. It is important to remark that the traveling waves theory will be relevant to our purposes for finding analytical solutions.

As we have mentioned above, Fisher [11] was a pioneer in the study of nonlinear parabolic models, but, at the same time, Kolmogorov et al. [15] developed the existence of solutions to (2) with a nonlinear reaction of the form $G(\tilde{v}) = \tilde{v}(1 - \tilde{v})$. Later on, this type of nonlinearity was widely considered for modeling in different scopes. Let us mention some of the previous studies in fluid mechanics that have attracted our interest: Shchelkin [16] considered the flow of gasses through a tube and developed the solution with a traveling wave analysis. Brailovsky et al. [17] modeled scenarios of a high hydraulic resistance and obtained a solution for when the flow passes through a porous medium.

The system represented by (1) and (2) was introduced by Gordon [1,2] to describe a flame evolution, and the main variables of temperature, pressure, and concentration of the deficient reactant were considered in the approach. Further on, Ghazaryan and Gordon [3] considered the linear transformation between temperature and pressure variables, and they also introduced the nonlinearity $G(\tilde{u}, \tilde{u}) = h\tilde{u} + (1 - h)\tilde{v}$, where $h \in [0, 1]$. It is noticed that this kind of nonlinearity is more general; indeed, if we take $h = 0$ and $h = 1$, then we can recover the models introduced by Fisher in [11] and Billingham and Needham in [18], respectively.

Our paper is structured to systematically address a new form of a model that aims at generalizing the second-order Laplacian term , as given in the baseline problems (1) and (2). Initially, we provide a mathematical formulation of the new problem to immediately focus on the aspects concerning the regularity and uniqueness of weak solutions. This is a critical step given the degenerate nature of diffusivity in our new problem. The regularity assessment ensures that the solutions are well behaved and follow smoothness criteria, which is crucial for the physical validity of the model. Simultaneously, we address the uniqueness of these solutions. To search for analytical solutions, we start by reformu-

lating our system by converting it into traveling wave solutions. This is performed so that, by employing topological principles alongside singular geometric perturbation theory, we carve out the analytical profiles of these traveling waves. To bolster the theoretical constructs, we incorporate a numerical assessment. This serves as a bridge between the purely theoretical world and some concrete scenarios, thus allowing us to validate our analytical findings. Hence, we ensure that our theoretical predictions hold up under numerical scrutiny, thereby providing a layer of reliability and realism to our study. Finally, our exploration culminates in the search for self-similar structured solutions. Self-similarity in this context provides a tool through whcih to understand the scaling and replication patterns of flame propagation.

2. Mathematical Formulation

In our approach to advancing the concept of flame diffusion beyond the conventional second-order Laplacian diffusion, we adopted the p-Laplacian operator as an alternative to the traditional Gaussian diffusion operator. This modification aims to provide a more comprehensive understanding of flame diffusion dynamics. Note that, if we take $p = 2$, then the classical Gaussian diffusion operator becomes a special case of the more general p-Laplacian diffusion. The p-Laplacian operator is of interest as its mathematical properties can closely fit with physical observations. For example, by taking $p \geq 2$, this operator satisfies the compactness property, thereby departing from compactly supported initial distributions. In addition, the p-Laplacian operator preserves the propagation energy in L^2 spaces (see [19,20]). The conception of using a p-Laplacian operator for modeling in applied problems is not new. Indeed, this operator has been used for modeling in the fields of economics (see [21–23]) or nonlinear elasticity (see [24–26]), which have been selected as representatives.

Another important purpose for introducing the p-Laplacian operator is related to increasing the versatility of the classical parabolic model in (1)–(3). Indeed, depending on the values of the $p-$parameter, we can observe the slow and fast effect of diffusion, which can be considered for the flame propagation in porous media. In actuality, the specific values for p in the p-Laplacian operator are obtained based on experimental observations and settings. This approach has been performed in fluid modeling in porous media thanks to the works of Smreker, who considered a $p-$Laplacian-derived diffusion to enhance the fidelity of Darcy's law (see [27,28]).

Based on the ideas introduced, let us consider System (1)–(3). Then, after introducing the p-Laplacian operator along with the bi-stable nonlinearity, we have

$$\frac{\partial \tilde{u}}{\partial t} = \frac{\partial}{\partial y}\left(\left(\frac{\partial \tilde{u}}{\partial y}\right)^{p-2}\frac{\partial \tilde{u}}{\partial y}\right) + \Big(1-\tilde{v}\Big)\Big(\tilde{v}-\mu\Big)\tilde{w}, \tag{4}$$

$$\frac{\partial \tilde{v}}{\partial t} = \frac{\partial}{\partial y}\left(\left(\frac{\partial \tilde{v}}{\partial y}\right)^{p-2}\frac{\partial \tilde{v}}{\partial y}\right) + \Big(1-\tilde{v}\Big)\Big(\tilde{v}-\mu\Big)\tilde{w}, \tag{5}$$

$$\tilde{w} = h\tilde{u} + \Big(1-h\Big)\tilde{v}, \tag{6}$$

where $y \in \mathbb{R}$, $t \in (0, T]$, $p > 2$ (which is typically the case in highly resistant porous media), $h \in (0,1)$, $\mu \in (0,1)$ $\tilde{u}(y,0) = \tilde{u}_0(y) > 0$ and $\tilde{v}(y,0) = \tilde{v}_0(y) > 0$. According to [3], the variable $\tilde{w}$ represents the temperature of the flame, while the variables $\tilde{u}, \tilde{v}$ are introduced as linear transformations of the temperature and pressure variables for the sake of analysis (again for additional insights, the reader is referred to [3]).

Our approach to solving the problem of $\tilde{u}(t,y)$ and $\tilde{v}(t,y)$ is grounded in mathematical theory and computation, and this was understood as a previous step before any physical or experimental modeling could be considered. This distinction is crucial, as our current analysis is not directly derived from, nor immediately applicable to, real-world experimental data or physical phenomena. Instead, we provide a mathematical representation

that allows us to explore and understand the theoretical aspects of the problem to check its mathematical adequacy for potential physical applications. And this is particularly relevant given the nonlinearities introduced in either the $p-$Laplacian diffusion and the reaction terms. Hence, a simple and direct question to answer is whether the solutions are analytically plausible—if they exist, they are unique, and they can be expressed analytically and numerically.

In this mathematical realm, our focus is on employing analytical and numerical techniques to investigate the properties of the solutions, such as boundedness and uniqueness. This involves applying theorems, principles, and computational algorithms to understand the behavior of these solutions within the defined theoretical framework, and this is to be performed previous to any physical or experimental orientation. The use of 2D or 3D plots and simulations is not to mimic real-world conditions or to predict experimental outcomes directly, but rather to visually interpret and validate the analytical solutions derived from the equations governing the problem. While our mathematical modeling may be regarded as a relevant step in the process of understanding the flame propagation phenomenon, it is just one part of a larger picture. Indeed, before these mathematical models can be applied to practical, real-world situations, they would need to be augmented with experimental data, physical validation, and would also need to be potentially adjusted to account for real-world complexities.

3. Previous and Preliminary Results

The following propositions are necessary for the assessment to be achieved, and they are reproduced from the references of [19,20].

We note that *Result* 1 given in [19] deals with non Lesbegue integrable functions. A norm is hence introduced for establishing a measuring of the growing solution trace (thereby providing conditions to determine the existence criteria of global solutions). The stated norm is (refer to [19]) as follows:

$$|||F|||_\rho = \sup_{R\geq\rho} R^{-\lambda} \int_{B_R(0)} |F|\, dy, \quad \lambda = 1 + \frac{p}{p-2}. \tag{7}$$

For simplicity, we consider that $\rho = 1$ in (7). For any given and finite $R \geq 1$, it can be easily checked that $|||F|||_\rho \leq ||F||_1$ in the classical ball $B_R(0)$, where the last norm is the Lebesgue L^1. Based on these arguments, which are introduced ad hoc, we adjust *Result 1* of [19] in Proposition 1.

Proposition 1. *Assuming that $u_0(y) \in L^1(B_R(0))$, for $y \in \mathbb{R}^d$ with $d \geq 1$, there exist a time $T(|||u_0|||_1)$ and a weak solution of the fundamental p-Laplacian equation $u_t = \nabla \cdot \left(|\nabla u|^{p-2}\nabla u\right)$ in $0 < t \leq T(|||u_0|||_1)$, such that the following expression holds:*

$$T(|||u_0|||_1) = A_1(p)|||u_0|||_1^{-(p-2)}. \tag{8}$$

In the classical ball domain $B_R(0)$, the following estimates apply:

$$|||u(\cdot,t)|||_1 \leq A_2(d,p)|||u_0|||_1 \leq A_2(d,p)||u_0||_1, \tag{9}$$

$$|u(y,t)| \leq A_3(d,p)t^{-c_0}R^{p(p-2)}|||u_0|||_1^{\frac{pc_0}{d}} \leq A_3(d,p)t^{-c_0}R^{p(p-2)}||u_0||_1^{\frac{pc_0}{d}}, \ |y| \leq R, \tag{10}$$

$$|\nabla u(y,t)| \leq A_4(d,p)t^{-\frac{(d+1)c_0}{d}}R^{\frac{2}{p-2}}|||u_0|||_1^{\frac{2c_0}{d}} \leq A_4(d,p)t^{-\frac{(d+1)c_0}{d}}R^{\frac{2}{p-2}}||u_0||_1^{\frac{2c_0}{d}}, \ |y| \leq R, \tag{11}$$

where $c_0 = \left(p-2+\frac{p}{d}\right)^{-1}$, and, by hypothesis, $|||u_0|||_1 \geq 1$. Note that $||u_0||_1$ is assessed in $B_R(0)$ and satisfies $||u_0||_{L^1(B_R(0))} \geq 1$ and $R \geq 1$. For the additional details concerning the constants A_1, A_2, A_3, and A_4, we refer the reader to [19].

The previous mentioned proposition was initially stated for $y \in \mathbb{R}^d$ (with $d \geq 1$) for $|y| < R$, and such results apply without inconsistencies in the spatial one-dimensional case.

Proposition 2. *Problems (4)–(6) admit a set of upper and flat solutions (which only depend on the t variable), and they are given by*

$$\tilde{u}_1 = \frac{hA_5^2A_6e^{-h(1+\mu)A_5t} - A_5}{hA_5A_6e^{-h(1+\mu)A_5t} - (1+h)}, \quad \tilde{v}_1 = \frac{hA_5}{hA_5A_6e^{-h(1+\mu)A_5t} - (1+h)}, \tag{12}$$

where $A_5 = \frac{\|v_0\|_r\left(h\|u_0\|_r - 1\right)}{h}$ *and* $A_6 = \frac{h\|u_0\|_r - 1}{\|v_0\|_r\left(h\|u_0\|_r - 1\right)}$.

Proof. To obtain the flat solutions that depend only on the t variable, we considered the following system:

$$\frac{\partial \tilde{u}}{\partial t} = \Big(1 - \tilde{v}\Big)\big(\tilde{v} - \mu\Big)\tilde{w}, \quad \frac{\partial \tilde{v}}{\partial t} = \Big(1 - \tilde{v}\Big)\big(\tilde{v} - \mu\Big)\tilde{w}, \quad \tilde{w} = h\tilde{u} + (1-h)\tilde{v}. \tag{13}$$

Given the parabolicity of the p-Laplacian operator for positive solutions (see [19,20] for dedicated discussions in this regard), we can state that the involved solutions, $\tilde{u}$, $\tilde{v}$, and $\tilde{w}$ are positive upon evolution and when departing from the positive initial data. Therefore, to find the upper solutions to (13), the following assessments hold:

$$\begin{aligned} \frac{\partial \tilde{u}}{\partial t} &= \Big(\tilde{v} + \mu\tilde{v} - (\tilde{v})^2 - \mu\Big)\tilde{w} \leq \Big(1 + \mu\Big)\tilde{v}\tilde{w} \\ \frac{\partial \tilde{v}}{\partial t} &= \Big(\tilde{v} + \mu\tilde{v} - (\tilde{v})^2 - \mu\Big)\tilde{w} \leq \Big(1 + \mu\Big)\tilde{v}\tilde{w} \\ \tilde{w} &= h\tilde{u} + \tilde{v} - h\tilde{v} \leq h\tilde{u} + \tilde{v}. \end{aligned} \tag{14}$$

Assuming $\tilde{u}_1$ and $\tilde{v}_1$ are two upper solutions, then the following system holds:

$$\frac{\partial \tilde{u}_1}{\partial t} = h\Big(1 + \mu\Big)\tilde{u}_1\tilde{v}_1 + \Big(1 + \mu\Big)(\tilde{v}_1)^2, \tag{15}$$

$$\frac{\partial \tilde{v}_1}{\partial t} = h\Big(1 + \mu\Big)\tilde{u}_1\tilde{v}_1 + \Big(1 + \mu\Big)(\tilde{v}_1)^2, \tag{16}$$

where the initial conditions for resembling Problems (15) and (16) are the same as the initial set of Equations (4)–(6). By subtracting (16) from (15) and letting $\tilde{f}(y,t) = \tilde{u}_1(y,t) - \tilde{v}_1(y,t)$, we have

$$\frac{\partial \tilde{f}}{\partial t} = 0. \tag{17}$$

After integrating and then using the initial conditions, we obtain

$$\tilde{f} = A_5, \tag{18}$$

where $A_5 = \|\tilde{u}_0\|_\infty - \|\tilde{v}_0\|_\infty$. After using $\tilde{v}_1 = \tilde{u}_1 - A_5$ in (15) and $\tilde{u}_1 = \tilde{v}_1 + A_5$ in (16), we obtain

$$\frac{\partial \tilde{u}_1}{\partial t} = h\Big(1 + \mu\Big)\tilde{u}_1(\tilde{u}_1 - A_5) + \Big(1 + \mu\Big)(\tilde{u}_1 - A_5)^2, \tag{19}$$

$$\frac{\partial \tilde{v}_1}{\partial t} = h\Big(1 + \mu\Big)\tilde{v}_1(\tilde{v}_1 + A_5) + \Big(1 + \mu\Big)(\tilde{v}_1)^2. \tag{20}$$

Problems (19) and (20) can be solved by standard means. We omitted the complete assessments in the sake of a concise representation, so that after operating we obtain the following solutions:

$$\tilde{u}_1 = \frac{hA_5^2A_6e^{-h(1+\mu)A_5t} - A_5}{hA_5A_6e^{-h(1+\mu)A_5t} - (1+h)}, \quad \tilde{v}_1 = \frac{hA_5}{hA_5A_6e^{-h(1+\mu)A_5t} - (1+h)}, \tag{21}$$

where A_5 and A_6 are obtained by using the initial conditions, so that $A_5 = \frac{\|v_0\|_r\left(h\|u_0\|_r - 1\right)}{h}$ and $A_6 = \frac{h\|u_0\|_r - 1}{\|v_0\|_r\left(h\|u_0\|_r - 1\right)}$. □

4. General Properties of Solutions

This section deals with topics concerning the regularity and uniqueness of solutions.

Firstly, the coming theorem shows that the weak solutions $\tilde{u}, \tilde{v}$ for Systems (4)–(6) are bounded.

Theorem 1. *Assuming that $\tilde{u}(y,t) \geq 0$ and $\tilde{v}(y,t) \geq 0$ are solutions to Problems (4)–(6), then these solutions are bounded in $t \in [0,\infty)$ and $y \in B_r$, where $0 \leq r \leq \infty$.*

Proof. Let us consider the weak formulation for Problems (4)–(6) based on a test function $\phi_1 \in C^\infty(\mathbb{R}\times[0,T]) \cap L^\infty(W^{1,p}(\mathbb{R}),[0,T])$ defined in $0 < s < t < T$, so that

$$\int_R \tilde{u}(t)\phi_1(t) = \int_R \tilde{u}(0)\phi_1(0) + \int_0^t \int_R \left(\tilde{u}\frac{\partial\phi_1}{\partial t} - \left|\frac{\partial\tilde{u}}{\partial y}\right|^{p-1}\frac{\partial\phi_1}{\partial y} + \left(1-\tilde{v}\right)\left(\tilde{v}-\mu\right)\tilde{w}\phi_1\right)ds, \tag{22}$$

$$\int_R \tilde{v}(t)\phi_1(t) = \int_R \tilde{v}(0)\phi_1(0) + \int_0^t \int_R \left(\tilde{v}\frac{\partial\phi_1}{\partial t} - \left|\frac{\partial\tilde{v}}{\partial y}\right|^{p-1}\frac{\partial\phi_1}{\partial y} + \left(1-\tilde{v}\right)\left(\tilde{v}-\mu\right)\tilde{w}\phi_1\right)ds. \tag{23}$$

To obtain the boundedness of the solutions, the following problem (named as p^{ϕ_1}) is defined:

$$\tilde{u}\frac{\partial\phi_1}{\partial t} - \left|\frac{\partial\tilde{u}}{\partial y}\right|^{p-1}\frac{\partial\phi_1}{\partial y} + \left(1-\tilde{v}\right)\left(\tilde{v}-\mu\right)\tilde{w}\phi_1 = 0, \tag{24}$$

and

$$\tilde{v}\frac{\partial\phi_1}{\partial t} - \left|\frac{\partial\tilde{v}}{\partial y}\right|^{p-1}\frac{\partial\phi_1}{\partial y} + \left(1-\tilde{v}\right)\left(\tilde{v}-\mu\right)\tilde{w}\phi_1 = 0, \tag{25}$$

where the test function is assumed to have the following structural form:

$$\phi_1(y,t) = \frac{e^{-c_1(t)}}{(1+|y|^2)^{c_2}}. \tag{26}$$

Consider $\lambda_1 \in \mathbb{R}^+$, where the following cut-off function $\tilde{\psi}_{\lambda_1}$ is defined (refer to [29] for additional insights):

$$\begin{gathered}\tilde{\psi}_{\lambda_1} \in C_0^\infty(\mathbb{R}), \qquad 0 \leq \tilde{\psi}_{\lambda_1} \leq 1,\\ \tilde{\psi}_{\lambda_1} = 1 \text{ for } y \in B_{r-\lambda_1} \text{ and } \tilde{\psi}_{\lambda_1} = 0 \text{ for } y \in \{R - B_{r-\lambda_1}\}.\end{gathered} \tag{27}$$

Then, we have the following:

$$|\nabla\tilde{\psi}_{\lambda_1}| \leq \frac{A_7}{\lambda_1}, \quad |\Delta\tilde{\psi}_{\lambda_1}| \leq \frac{A_7}{\lambda_1^2}. \tag{28}$$

By multiplying (24) and (25) by $\tilde{\psi}_{\lambda_1}$ and integrating, the following holds for $(y,t)\times B_r$ with $0<s\leq t<\infty$:

$$\int_0^t\int_{B_r}\tilde{u}\frac{\partial\phi_1}{\partial s}\tilde{\psi}_{\lambda_1}ds=\int_0^t\int_{B_r}\Big(\Big|\frac{\partial\tilde{u}}{\partial y}\Big|^{p-1}\frac{\partial\phi_1}{\partial y}\tilde{\psi}_{\lambda_1}-\Big(1-\tilde{v}\Big)\Big(\tilde{v}-\mu\Big)\tilde{w}\phi_1\tilde{\psi}_{\lambda_1}\Big)ds, \tag{29}$$

and

$$\int_0^t\int_{B_r}\tilde{v}\frac{\partial\phi_1}{\partial s}\tilde{\psi}_{\lambda_1}ds=\int_0^t\int_{B_r}\Big(\Big|\frac{\partial\tilde{v}}{\partial y}\Big|^{p-1}\frac{\partial\phi_1}{\partial y}\tilde{\psi}_{\lambda_1}-\Big(1-\tilde{v}\Big)\Big(\tilde{v}-\mu\Big)\tilde{w}\phi_1\tilde{\psi}_{\lambda_1}\Big)ds, \tag{30}$$

where ϕ_1, $\frac{\partial\phi_1}{\partial s}$, and $\tilde{\psi}_{\lambda_1}$ are continuously smooth functions that approach to zero at infinity.

To show the boundedness of the solutions, we shall show that the integral $\int_0^t\int_{B_r}\tilde{u}\frac{\partial\phi_1}{\partial s}\tilde{\psi}_{\lambda_1}ds$ and $\int_0^t\int_{B_r}\tilde{v}\frac{\partial\phi_1}{\partial s}\tilde{\psi}_{\lambda_1}ds$ are finite. To this end, we used Proposition 1, Proposition 2, and the test function ϕ_1, which are given in (26). Then, it holds that

$$\begin{aligned}
\int_0^t\int_{B_r}\Big|\frac{\partial\tilde{u}}{\partial y}\Big|^{p-1}\frac{\partial\phi_1}{\partial y}\psi_{\lambda_1}ds &\leq \int_0^t\int_{B_r}\Big(A_4^{p-1}t^{-2c_0(p-1)}|y|^{2+\frac{2}{p-2}}\|u_0\|_1^{2c_0(p-1)}\\
&+\Big(\frac{hA_5^2A_6e^{-h(1+\mu)A_5t}-A_5}{hA_5A_6e^{-h(1+\mu)A_5t}-(1+h)}\Big)^{p-1}\Big)\frac{2|-c_2||y|e^{-c_1(t)}}{(1+|y|^2)^{c_2+1}}\tilde{\psi}_{\lambda_1}ds\\
&\leq \int_0^t\int_{B_r}\Big(A_4^{p-1}t^{-2c_0(p-1)}|y|^{1+\frac{2}{p-2}-2c_2}\|u_0\|_1^{2c_0(p-1)}\\
&+\Big(\frac{hA_5^2A_6e^{-h(1+\mu)A_5t}-A_5}{hA_5A_6e^{-h(1+\mu)A_5t}-(1+h)}\Big)^{p-1}y^{-1-2c_2}\Big)2c_2e^{-c_1(t)}\tilde{\psi}_{\lambda_1}ds\\
&\leq \int_0^t\int_{B_r}\Big(A_4^{p-1}t^{-2c_0(p-1)}|y|^{1+\frac{2}{p-2}-2c_2}\|u_0\|_1^{2c_0(p-1)}\\
&+\Big(\frac{hA_5^2A_6e^{-h(1+\mu)A_5t}-A_5}{hA_5A_6e^{-h(1+\mu)A_5t}-(1+h)}\Big)^{p-1}y^{-1-2c_2}\Big)2c_2e^{-c_1(t)}\frac{A_7}{\lambda_1}ds\\
&\leq \int_0^t\int_{B_r}\Big(A_4^{p-1}t^{-2c_0(p-1)}|y|^{\frac{2}{p-2}-2c_2}\|u_0\|_1^{2c_0(p-1)}\\
&+\Big(\frac{hA_5^2A_6e^{-h(1+\mu)A_5t}-A_5}{hA_5A_6e^{-h(1+\mu)A_5t}-(1+h)}\Big)^{p-1}y^{-2-2c_2}\Big)2c_2A_7e^{-c_1(t)}ds.
\end{aligned} \tag{31}$$

The asymptotic convergence of the last integral requires us to consider $c_2\geq\frac{1}{p-2}=c_3$.

Similarly,

$$\begin{aligned}
\int_0^t\int_{B_r}\Big|\frac{\partial\tilde{v}}{\partial y}\Big|^{p-1}\frac{\partial\phi_1}{\partial y}\psi_{\lambda_1}ds &\leq \int_0^t\int_{B_r}\Big(A_4^{p-1}t^{-2c_0(p-1)}|y|^{\frac{2}{p-2}-2c_2}\|u_0\|_1^{2c_0(p-1)}\\
&+\Big(\frac{hA_5}{hA_5A_6e^{-h(1+\mu)A_5t}-(1+h)}\Big)^{p-1}y^{-2-2c_2}\Big)2c_2A_7e^{-c_1(t)}ds.
\end{aligned} \tag{32}$$

This last integral is asymptotically convergent if $c_2\geq\frac{1}{p-2}=c_4$.

Again, in using (3) and Propositions 1 and 2 , the assessment of the last term in (29) is performed as follows:

$$
\begin{aligned}
&\int_0^t \int_{B_r} \Big(1-\tilde{v}\Big)\Big(\tilde{v}-\mu\Big)\tilde{w}\phi_1\tilde{\psi}_{\lambda_1} ds \\
\leq\ & h(1+\mu)\int_0^t \int_{B_r} \tilde{u}\tilde{v}\phi_1\tilde{\psi}_{\lambda_1} ds + (1+\mu)\int_0^t \int_{B_r} \tilde{v}^2\phi_1\tilde{\psi}_{\lambda_1} ds \\
\leq\ & h(1+\mu)\int_0^t \int_{B_r} \Big(A_3 t^{-c_0}|y|^{p(p-2)}\|u_0\|_1^{pc_0} \\
+\ & \frac{hA_5^2A_6e^{-h(1+\mu)A_5t}-A_5}{hA_5A_6e^{-h(1+\mu)A_5t}-(1+h)}\Big)\Big(A_3 t^{-c_0}|y|^{p(p-2)}\|v_0\|_1^{pc_0} \\
+\ & \frac{hA_5}{hA_5A_6e^{-h(1+\mu)A_5t}-(1+h)}\Big)\frac{e^{-c_1(t)}}{(1+|y|^2)^{c_2}}\tilde{\psi}_{\lambda_1} ds \\
+\ & (1+\mu)\int_0^t \int_{B_r} \Big(A_3^2 t^{-2c_0}|y|^{p(p-2)}\|v_0\|_1^{2pc_0} \\
+\ & \Big(\frac{hA_5}{hA_5A_6e^{-h(1+\mu)A_5t}-(1+h)}\Big)^2\Big)\frac{e^{-c_1(t)}}{(1+|y|^2)^{c_2}}\tilde{\psi}_{\lambda_1} ds \\
\leq\ & h(1+\mu)\int_0^t \int_{B_r} \Big(A_3 t^{-c_0}|y|^{p(p-2)}\|u_0\|_1^{pc_0} \\
+\ & \frac{hA_5^2A_6e^{-h(1+\mu)A_5t}-A_5}{hA_5A_6e^{-h(1+\mu)A_5t}-(1+h)}\Big)\Big(A_3 t^{-c_0}|y|^{p(p-2)}\|v_0\|_1^{pc_0} \\
+\ & \frac{hA_5}{hA_5A_6e^{-h(1+\mu)A_5t}-(1+h)}\Big)y^{-2c_2}e^{-c_1(t)}\tilde{\psi}_{\lambda_1} ds \\
+\ & (1+\mu)\int_0^t \int_{B_r} \Big(A_3^2 t^{-2c_0}|y|^{p(p-2)}\|v_0\|_1^{2pc_0} \\
+\ & \Big(\frac{hA_5}{hA_5A_6e^{-h(1+\mu)A_5t}-(1+h)}\Big)^2\Big)y^{-2c_2}e^{-c_1(t)}\tilde{\psi}_{\lambda_1} ds. \qquad (33)
\end{aligned}
$$

Indeed, both integrals above converge asymptotically for $c_2 \geq \frac{P(p-2)-1}{2} = c_5$.

The integrals overall convergence, which is represented in Expressions (29)–(33), requires taking

$$c_2 \geq \max(c_3, c_4, c_5). \qquad (34)$$

In coming back to (29) and (30), as well as considering any value of $t > 0$ and taking $r \to \infty$, we have

$$0 \leq \int_0^t \int_{B_r} \tilde{u}\frac{\partial\phi_1}{\partial s}\tilde{\psi}_{\lambda_1} ds \leq M_1, \qquad (35)$$

and

$$0 \leq \int_0^t \int_{B_r} \tilde{v}\frac{\partial\phi_1}{\partial s}\tilde{\psi}_{\lambda_1} ds \leq M_2, \qquad (36)$$

where M_1 and M_2 are finite given the fact that the stated integrals converge asymptotically upon selection of the mentioned c_2 value. After using (35) and (36) into (22) and (23), as well as using the boundness property of the test function ϕ_1, we can conclude that $\tilde{u}$ and $\tilde{v}$ are bounded in $B_r \times [0, \infty)$. □

The next intention is to prove the uniqueness of the solutions to the problem (4)–(6). For this, the following theorem provides a result about the uniqueness.

Theorem 2. *Suppose that $\tilde{u}_1(y,t) \geq 0$, that $\tilde{v}_1(y,t) \geq 0$ constitute a maximal set of weak solutions, and that $\tilde{u}_2(y,t) \geq 0$, $\tilde{v}_2(y,t) \geq 0$ constitute a minimal set of weak solutions to* (4)

and (5) *in* $B_r \times (0,T)$, *where* $B_r \in \mathbb{R}$ *is the classical ball. Then, the maximal and the minimal solutions coincide for* $r \gg 1$, *i.e the solution is unique.*

Proof. Assuming that $\tilde{u}_1$ and $\tilde{v}_1$ are the maximal solution of (4) and (5), such that

$$\tilde{u}_1(y,0) = u_0(y) + \epsilon, \;\; \tilde{v}_1(y,0) = v_0(y) + \epsilon, \tag{37}$$

where $\epsilon > 0$, then the functions $\tilde{u}_2$ and $\tilde{v}_2$ are the minimal solution of (1) and (2) with the initial conditions

$$\tilde{u}_2(y,0)) = u_0(y), \;\; \tilde{v}_2(y,0) = v_0(y). \tag{38}$$

Given a test function $\phi_1 \in C^\infty(R \times [0,T]) \cap L^\infty(W^{1,p}(\mathbb{R}),[0,T])$, then the following holds:

$$\int_{B_r} \tilde{u}_1(t)\phi_1(t) = \int_{B_r} \tilde{u}_1(0)\phi_1(0) + \int_0^t \int_{B_r} \Big(\tilde{u}_1 \frac{\partial \phi_1}{\partial s} - \Big|\frac{\partial \tilde{u}_1}{\partial y}\Big|^{p-1} \frac{\partial \phi_1}{\partial y} + \Big(1-\tilde{v}_1\Big)\Big(\tilde{v}_1 - \mu\Big)\tilde{w}_1\phi_1\Big) ds, \tag{39}$$

$$\int_{B_r} \tilde{v}_1(t)\phi_1(t) = \int_{B_r} \tilde{v}_1(0)\phi_1(0) + \int_0^t \int_{B_r} \Big(\tilde{v}_1 \frac{\partial \phi_1}{\partial s} - \Big|\frac{\partial \tilde{v}_1}{\partial y}\Big|^{p-1} \frac{\partial \phi_1}{\partial y} + \Big(1-\tilde{v}_1\Big)\Big(\tilde{v}_1 - \mu\Big)\tilde{w}_1\phi_1\Big) ds, \tag{40}$$

and

$$\int_{B_r} \tilde{u}_2(t)\phi_1(t) = \int_{B_r} \tilde{u}_2(0)\phi_1(0) + \int_0^t \int_{B_r} \Big(\tilde{u}_2 \frac{\partial \phi_1}{\partial s} - \Big|\frac{\partial \tilde{u}_2}{\partial y}\Big|^{p-1} \frac{\partial \phi_1}{\partial y} + \Big(1-\tilde{v}_2\Big)\Big(\tilde{v}_2 - \mu\Big)\tilde{w}_2\phi_1\Big) ds, \tag{41}$$

$$\int_{B_r} \tilde{v}_2(t)\phi_1(t) = \int_{B_r} \tilde{v}_2(0)\phi_1(0) + \int_0^t \int_{B_r} \Big(\tilde{v}_2 \frac{\partial \phi_1}{\partial s} - \Big|\frac{\partial \tilde{v}_2}{\partial y}\Big|^{p-1} \frac{\partial \phi_1}{\partial y} + \Big(1-\tilde{v}_2\Big)\Big(\tilde{v}_2 - \mu\Big)\tilde{w}_2\phi_1\Big) ds. \tag{42}$$

From the boundedness conditions of the solutions obtained in Theorem 1, we can state the following integrals on the finiteness:

$$\begin{aligned} &\int_0^t \int_{B_r} \Big|\frac{\partial \tilde{u}_1}{\partial y}\Big|^{p-1} \frac{\partial \phi_1}{\partial y} ds = A_8, \quad \int_0^t \int_{B_r} \Big|\frac{\partial \tilde{u}_2}{\partial y}\Big|^{p-1} \frac{\partial \phi_1}{\partial y} ds = A_9, \\ &\int_0^t \int_{B_r} \Big|\frac{\partial \tilde{v}_1}{\partial y}\Big|^{p-1} \frac{\partial \phi_1}{\partial y} ds = A_{10}, \quad \int_0^t \int_{B_r} \Big|\frac{\partial \tilde{v}_2}{\partial y}\Big|^{p-1} \frac{\partial \phi_1}{\partial y} ds = A_{11}. \end{aligned} \tag{43}$$

Also, we have

$$\int_0^t \int_{B_r} \Big(1-\tilde{v}_1\Big)\Big(\tilde{v}_1 - \mu\Big)\tilde{w}_1\phi_1 ds \le h(1+\mu) \int_0^t \int_{B_r} \tilde{u}_1\tilde{v}_1\phi_1 ds + (1+\mu) \int_0^t \int_{B_r} \tilde{v}_1^2\phi_1 ds, \tag{44}$$

and

$$\int_0^t \int_{B_r} \Big(1-\tilde{v}_2\Big)\Big(\tilde{v}_2 - \mu\Big)\tilde{w}_2\phi_1 ds \le h(1+\mu) \int_0^t \int_{B_r} \tilde{u}_2\tilde{v}_2\phi_1 ds + (1+\mu) \int_0^t \int_{B_r} \tilde{v}_2^2\phi_1 ds. \tag{45}$$

After using (44)–(47), Expressions (39)–(42) become

$$\begin{aligned} \int_{B_r} \tilde{u}_1(t)\phi_1(t) &= \int_{B_r} \tilde{u}_1(0)\phi_1(0) + \int_0^t \int_{B_r} \tilde{u}_1 \frac{\partial \phi_1}{\partial s} ds \\ &+ h(1+\mu) \int_0^t \int_{B_r} \tilde{u}_1\tilde{v}_1\phi_1 ds + (1+\mu) \int_0^t \int_{B_r} \tilde{v}_1^2\phi_1 ds - A_8, \end{aligned} \tag{46}$$

$$\begin{aligned}\int_{B_r} \tilde{v}_1(t)\phi_1(t) &= \int_{B_r} \tilde{v}_1(0)\phi_1(0) + \int_0^t \int_{B_r} \tilde{v}_1 \frac{\partial \phi_1}{\partial s} ds \\ &+ h(1+\mu)\int_0^t \int_{B_r} \tilde{u}_1\tilde{v}_1\phi_1 ds + (1+\mu)\int_0^t \int_{B_r} \tilde{v}_1^2\phi_1 ds - A_9, \end{aligned} \tag{47}$$

and

$$\begin{aligned}\int_{B_r} \tilde{u}_2(t)\phi_1(t) &= \int_{B_r} \tilde{u}_2(0)\phi_1(0) + \int_0^t \int_{B_r} \tilde{u}_2 \frac{\partial \phi_1}{\partial s} ds \\ &+ h(1+\mu)\int_0^t \int_{B_r} \tilde{u}_2\tilde{v}_2\phi_1 ds + (1+\mu)\int_0^t \int_{B_r} \tilde{v}_2^2\phi_1 ds - A_{10}, \end{aligned} \tag{48}$$

$$\begin{aligned}\int_{B_r} \tilde{v}_2(t)\phi_1(t) &= \int_{B_r} \tilde{v}_2(0)\phi_1(0) + \int_0^t \int_{B_r} \tilde{v}_2 \frac{\partial \phi_1}{\partial s} ds \\ &+ h(1+\mu)\int_0^t \int_{B_r} \tilde{u}_2\tilde{v}_2\phi_1 ds + (1+\mu)\int_0^t \int_{B_r} \tilde{v}_2^2\phi_1 ds - A_{11}. \end{aligned} \tag{49}$$

In particular, we define the test function as follows:

$$\phi_1(y,t) = \frac{e^{-c_6 t}}{(1+|y|^2)^{c_2}}. \tag{50}$$

By subtracting (48) from (46) and (49) from (47), as well as taking $\epsilon \to 0$, we have

$$\begin{aligned}&\int_{B_r} \Big(\tilde{u}_1 t) - \tilde{u}_2(t)\Big)\phi_1(t) \le -c_6 \int_0^t \int_{B_r} \Big(\tilde{u}_1 - \tilde{u}_2\Big)\phi_1 ds + A_{10} - A_8 \\ &+ h(1+\mu)\int_0^t \int_{B_r} \Big(\tilde{u}_1\tilde{v}_1 - \tilde{u}_2\tilde{v}_2\Big)\phi_1 ds + (1+\mu)\int_0^t \int_{B_r} \Big(\tilde{v}_1^2 - \tilde{v}_2^2\Big)\phi_1 ds, \end{aligned} \tag{51}$$

and

$$\begin{aligned}&\int_{B_r} \Big(\tilde{v}_1 t) - \tilde{v}_2(t)\Big)\phi_1(t) \le -c_6 \int_0^t \int_{B_r} \Big(\tilde{v}_1 - \tilde{v}_2\Big)\phi_1 ds + A_{11} - A_9 \\ &+ h(1+\mu)\int_0^t \int_{B_r} \Big(\tilde{u}_1\tilde{v}_1 - \tilde{u}_2\tilde{v}_2\Big)\phi_1 ds + (1+\mu)\int_0^t \int_{B_r} \Big(\tilde{v}_1^2 - \tilde{v}_2^2\Big)\phi_1 ds. \end{aligned} \tag{52}$$

Considering the form of Test Function as given in (50), we can choose c_6 such that

$$-c_6\Big(\tilde{u}_1 - \tilde{u}_2\Big)\phi_1 \le 0 \text{ and } -c_6\Big(\tilde{v}_1 - \tilde{v}_2\Big)\phi_1 \le 0. \tag{53}$$

When differentiating (51) and (52) with respect to t and then subtracting, we have

$$\frac{d}{dt}\left(\int_{B_r} \Big(\tilde{u}_1(t) - \tilde{u}_2(t)\Big)\phi_1(t) - \int_{B_r} \Big(\tilde{v}_1(t) - \tilde{v}_2(t)\Big)\phi_1(t)\right) \le 0, \tag{54}$$

where we used (53). After integration, we obtain

$$\int_{B_r} \Big(\tilde{u}_1(t) - \tilde{u}_2(t)\Big)\phi_1(t) - \int_{B_r} \Big(\tilde{v}_1(t) - \tilde{v}_2(t)\Big)\phi_1(t) \le A_{12}. \tag{55}$$

The constant A_{12} can be assessed asymptotically by considering that Test Function (50) verifies $\phi_1(|y| \to \infty) \to 0$. Then, we have

$$\tilde{u}_1 - \tilde{u}_2 = \tilde{v}_1 - \tilde{v}_2. \tag{56}$$

Expression (56) can be further assessed by using the initial data as follows:

$$u_0 + \epsilon - u_0 = \epsilon, \tag{57}$$

where ϵ can be taken as sufficiently small so that

$$\tilde{u}_1 - \tilde{u}_2 = \tilde{v}_1 - \tilde{v}_2 \to 0, \tag{58}$$

which implies that the distance between solutions can be made sufficiently small so as to support $\tilde{u}_1 = \tilde{u}_2$ and $\tilde{v}_1 = \tilde{v}_2$, leading to uniqueness of solutions. □

Numerical Simulation of the Weak Solutions

The intention of the numerical simulation in this section is to provide further evidence to support the boundedness of the solutions introduced in Theorem 1 and the uniqueness shown in Theorem 2. To perform a numerical simulation to obtain weak solutions, we followed a methodological approach: Firstly, it was required to discretize the domain of integration. Since the domain was $\mathbb{R} \times [0, T]$, we assumed a finite interval; for example, $[-L, L]$ but with a large L. Afterward, the integro-differential equations given in the weak formulation in Theorem 1, i.e., Equations (22) and (23), needed to be discretized. This can be conducted using methods like the Finite Difference Method (FDM), Finite Element Method (FEM), etc. In our case, the combination of temporal discretization using FDM and spatial discretization with numerical integration (Simpson's rule) allowed for an approximate solution of the weak formulation of the problem, thus leading to a numerical representation of the solution to Equations (22) and (23) over the discretized time–space domain. To provide detailed insights on how the FDM was used in the numerical simulation for obtaining weak solutions, let us break down the process:

Temporal Discretization with FDM:

1. **Grid Creation:** The time domain $[0, T]$ was divided into small, discrete time steps, thus creating a temporal grid.
2. **Derivative Approximation:** FDM approximates derivatives in the equations by using differences between successive grid points. A first-order temporal derivative was employed and approximated as $\frac{f(t+\Delta t)-f(t)}{\Delta t}$.
3. **Iterative Time Stepping:** Starting from the initial conditions, the solution was iteratively computed for each time step. The information from the previous time step (or steps, depending on the order of the method) was used to calculate the solution at the next time step.

Spatial Discretization with Simpson's Rule for Numerical Integration:

1. **Domain Discretization:** The spatial domain $[-L, L]$ was discretized into smaller segments, thereby forming a spatial grid.
2. **Integration using Simpson's Rule:** Simpson's Rule was applied to approximate the integrals in the weak formulation on the discretized spatial domain. This rule was particularly effective as the involved functions were indeed shown as smooth functions. Simpson's Rule provided a good balance between accuracy and computational efficiency.

Combining Temporal and Spatial Discretization:

- The discrete spatial domain affects the computation in each time step. At every step in time, the spatially discretized equations were solved to update the solution throughout the spatial domain.
- This combined approach allowed for the evolution of the solution over time while maintaining spatial accuracy.

Additionally, we implemented the test function, which is given in (26), with $c_1(t) = t$ and $c_2 = 1$. Given the discretized equations and the test function, we could solve for $\tilde{u}$ and $\tilde{v}$. This involved setting up a system of equations and solving them, typically through using numerical methods. The selected parameters values were $\mu = 0.5$ and $p = 3$.

The main computation loop involved iterating over each time step (excluding the initial condition at time zero). For each time step we performed the following: The values

of $\tilde{u}$ and $\tilde{v}$ at the previous time step were used to calculate the integrals in Equations (22) and (23). Simpson's Rule, as implemented via the *simps* function from the *scipy.integrate* Python module, was used for the numerical integration over the spatial domain. This involved computing the integral of the product of the solution functions, their gradients, and the test function ϕ_1, as specified in the weak formulation given in Equations (22) and (23). The calculated integrals were then used to update the values of $\tilde{u}$ and $\tilde{v}$ for the current time step.

Based on the provided 3D plots in Figure 1, we can discuss the aspects of boundedness and uniqueness of the solutions to validate the assessments conducted in Theorems 1 and 2. First, the plots do not show any extreme values or spikes that would suggest unbounded behavior within the time interval and spatial domain (recall the L value considered was 1000 and $T = 150$). This aligns with the results obtained in Theorem 1. In terms of uniqueness, Figure 1 provides a representation that is consistent with the unique solution shown in Theorem 2.

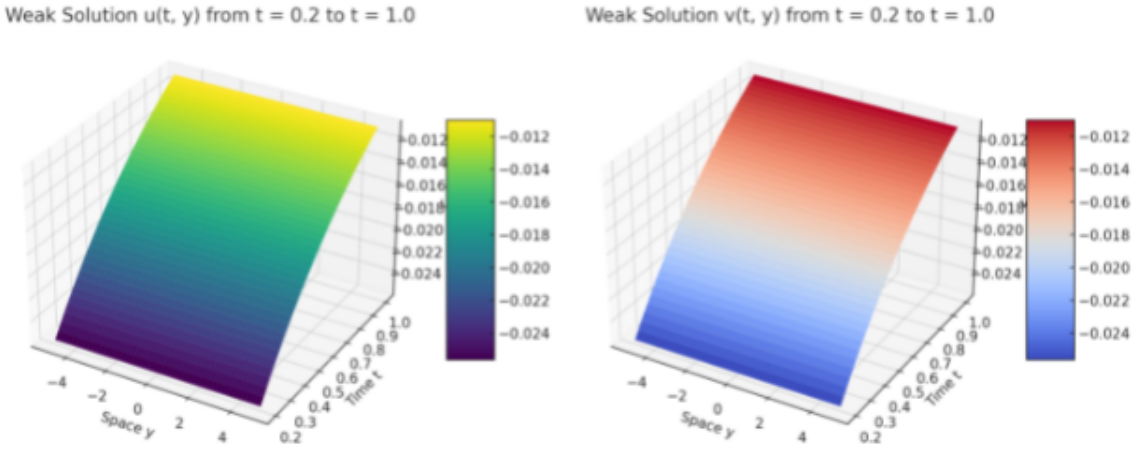

Figure 1. (**Left plot**): A 3D visualization of the weak solution $\tilde{u}(t, y)$. This plot illustrates the behavior of solution $\tilde{u}$ over the discretized spatial domain y and within the specified time interval $t = 0.2$ to $t = 1.0$. The surface's contours and color gradients represent the variations and evolution of $\tilde{u}$ as time progresses. (**Right plot**): A 3D visualization of the weak solution $\tilde{v}(t, y)$. This plot depicts the dynamic changes in the solution $\tilde{v}$ in the spatial domain y along the x-axis over the same time range as in Figure 1. The plot provides a visual representation of how $\tilde{v}$ evolves spatially and temporally, with color changes indicating the solution's variation over time. The L value considered was 1000 and the $T = 150$, while we only selected a representative sub-interval for accurate plotting. Note that the solutions exhibited a similar behavior in the whole integration domain compared to the behavior provided in the plots.

The consistency between the numerical visualization and the analytical proofs underscores the reliability of the simulation approach and the methods used. It confirms that the numerical methods and discretization strategies employed in the simulation are well aligned with the theoretical underpinnings of the problem, and we have analytically established this by visually representing the unique and bounded solutions.

5. Traveling Wave Analysis

Our target was to then characterize the solutions to Systems (4)–(6) by using the techniques focused on traveling waves. In the context of flame evolution, these solutions represent a scenario where the shape of the flame front does not change, though it does move at a constant speed. This stable wave-like behavior captures the relevant characteristics of flame dynamics such as speed, direction, and shape, thereby providing insights into the propagation of flames in porous media. Moreover, traveling wave solutions allow for a reduction in complex, nonlinear time and spatial dependent problems into systems of

ordinary differential equations depending on a simpler variable. As such, firstly, we let $\tilde{u}(y,t) = \tilde{F}_1(\zeta)$, $\tilde{v}(y,t) = \tilde{F}_2(\zeta)$, $\zeta = y - ct \in \mathbb{R}$, where c shows the speed of the traveling waves. For the reformulation of Systems (4)–(6) to the traveling wave domain, we have

$$-c\tilde{F}_1' = (p-1)\left(\tilde{F}_1'\right)^{p-2}\tilde{F}_1'' + \left(1-\tilde{F}_2\right)\left(\tilde{F}_2-\mu\right)\left(h\tilde{F}_1 + (1-h)\tilde{F}_2\right) \tag{59}$$

and

$$-c\tilde{F}_2' = (p-1)\left(\tilde{F}_2'\right)^{p-2}\tilde{F}_2'' + \left(1-\tilde{F}_2\right)\left(\tilde{F}_2-\mu\right)\left(h\tilde{F}_1 + (1-h)\tilde{F}_2\right). \tag{60}$$

The traveling waves problem was analyzed with the density and flux functions, which were defined as follows:

$$\tilde{X}_1 = \tilde{F}_1(\zeta), \quad \tilde{Y}_1 = \left(\tilde{F}_1'(\zeta)\right)^{p-1}, \quad \tilde{X}_2 = \tilde{F}_2(\zeta), \quad \tilde{Y}_2 = \left(\tilde{F}_2'(\zeta)\right)^{p-1}, \tag{61}$$

so that the following held

$$\begin{aligned}
\tilde{X}_1' &= \tilde{Y}_1^{\frac{1}{p-1}}, \\
\tilde{Y}_1' &= -c\tilde{Y}_1^{\frac{1}{p-1}} - \left(1-\tilde{X}_2\right)\left(\tilde{X}_2-\mu\right)\left(h\tilde{X}_1 + (1-h)\tilde{X}_2\right), \\
\tilde{X}_2' &= \tilde{Y}_2^{\frac{1}{p-1}}, \\
\tilde{Y}_2' &= -c\tilde{Y}_2^{\frac{1}{p-1}} - \left(1-\tilde{X}_2\right)\left(\tilde{X}_2-\mu\right)\left(h\tilde{X}_1 + (1-h)\tilde{X}_2\right).
\end{aligned} \tag{62}$$

The stationary conditions were $(\tilde{X}_1, \tilde{Y}_1, \tilde{X}_2, \tilde{Y}_2) = (N_2, 0, \mu, 0)$ and $(\tilde{X}_1, \tilde{Y}_1, \tilde{X}_2, \tilde{Y}_2) = (N_1, 0, 1, 0)$, where $N_2 = -\frac{(1-h)\mu}{h}$ and $N_1 = -\frac{1-h}{h}$ constitute the critical points of (62). Based on this, the following Lemma holds:

Lemma 1. *The critical points $(N_2, 0, \mu, 0)$ and $(N_1, 0, 1, 0)$ represent two degenerate nodes, with the following properties:*

- *If $h(\mu - N_2) > \mu$, there exist three negative and one null eigenvalues.*
- *If $h(\mu - N_2) \leq \mu$, there exist two negative, one positive, and one null eigenvalues.*
- *If $h(1 - N_1) \leq 1$, there exist three negative and one null eigenvalues.*
- *If $h(1 - N_1) > 1$, there exist two negative, one positive, and one null eigenvalues.*

In addition, there exists a Hopf bifurcation that is characterized by a minimum value in the traveling wave speed. Hence, for any $c < c_{min}$, the profiles of traveling waves are oscillating in the proximity of the critical points.

Proof. In the proximity of $(N_2, 0, \mu, 0)$, consider the following approximation:

$$\bar{X}_2 = \mu - \tilde{X}_2, \quad \bar{X}_2 \ll 1. \tag{63}$$

Then, in such proximity, System (62) is expressed as follows:

$$\begin{pmatrix} \tilde{X}_1' \\ \tilde{Y}_1' \\ \bar{X}_2' \\ \tilde{Y}_2' \end{pmatrix} = \begin{pmatrix} 0 & 1 & 0 & 0 \\ 0 & -c & (1-\mu)\left(-h(\mu - N_2) + \mu\right) & 0 \\ 0 & 0 & 0 & 1 \\ 0 & 0 & (1-\mu)\left(-h(\mu - N_2) + \mu\right) & -c \end{pmatrix} \begin{pmatrix} \tilde{X}_1 \\ \tilde{Y}_1 \\ \bar{X}_2 \\ \tilde{Y}_2 \end{pmatrix}. \tag{64}$$

The corresponding eigenvalues in vector form are given as

$$\left(0, -c, -\frac{c}{2} + \frac{1}{2}\sqrt{c^2 + 4\left(1-\mu\right)\left[-h(\mu - N_2) + \mu\right]}, -\frac{c}{2} - \frac{1}{2}\sqrt{c^2 + 4\left(1-\mu\right)\left[-h(\mu - N_2) + \mu\right]}\right).$$

The purely monotone eigenvalues are given for the following:

$$N_2 \geq \frac{-c^2 - 4\mu(1-\mu)(1-h)}{4h(1-\mu)}. \tag{65}$$

Furthermore, we stated that there exists a minimum traveling wave speed c_{min}, so that for any $c \geq c_{min}$, the profiles of the traveling waves were monotone decreasing or increasing (no oscillating), which can be obtained by a direct computation in Expression (65) as

$$c_{min} = 2\sqrt{(1-\mu)(h(\mu - N_2) - \mu)}. \tag{66}$$

Note that the computed eigenvalues lead directly to the cases stated in Lemma 1. The flow associated to the null eigenvalue is $\tilde{X}_1 = N_2$ and $\tilde{X}_2 = 0$, as well as (by translation) $\tilde{X}_1 = N_2$ and $\tilde{X}_2 = \mu$. Hence, for $c < c_{min}$, a Hopf bifurcation occurs according to the form of the obtained eigenvalues.

Note that after computation of the corresponding flows by direct operations, the following leading terms are computed in the proximity of the critical point $\left(\tilde{X}_1, \tilde{Y}_1, \tilde{X}_2, \tilde{Y}_2\right) = \left(N_2, 0, \mu, 0\right)$:

$$\tilde{X}_1 = C_3 e^{\lambda t}, \quad \tilde{X}_2 = C_4 e^{\lambda t}, \tag{67}$$

which shows the regular convergence of the traveling wave solutions in the proximity of the critical point. Note that $C_3 \in \mathbb{R}$, $C_4 \in \mathbb{R}$, and λ refer to each form of the eigenvalues obtained from the matrix detailed in (64).

Now, in the proximity of $(N_1, 0, 1, 0)$, we considered the following:

$$\bar{X}_2 = 1 - \tilde{X}_2, \quad \tilde{X}_2 \ll 1. \tag{68}$$

Then, in such proximity, System (11) was expressed as follows:

$$\begin{pmatrix} \tilde{X}_1' \\ \tilde{Y}_1' \\ \tilde{X}_2' \\ \tilde{Y}_2' \end{pmatrix} = \begin{pmatrix} 0 & 1 & 0 & 0 \\ 0 & -c & (1-\mu)\left(h(1-N_1)-1\right) & 0 \\ 0 & 0 & 0 & 1 \\ 0 & 0 & (1-\mu)\left(h(1-N_1)-1\right) & -c \end{pmatrix} \begin{pmatrix} \tilde{X}_1 \\ \tilde{Y}_1 \\ \tilde{X}_2 \\ \tilde{Y}_2 \end{pmatrix}. \tag{69}$$

The corresponding eigenvalues were given by

$$\left(0,\ -c,\ -\frac{c}{2} + \frac{1}{2}\sqrt{c^2 + 4\Big(1-\mu\Big)\Big[h(1-N_1)-1\Big]},\ -\frac{c}{2} - \frac{1}{2}\sqrt{c^2 + 4\Big(1-\mu\Big)\Big[h(1-N_1)-1\Big]}\right).$$

The purely monotone eigenvalues were given for the following:

$$N_1 \leq \frac{c^2 + 4(1-\mu)(h-1)}{4h(1-\mu)}. \tag{70}$$

Again, we state that there exists a minimum traveling wave speed c_{min}, such that for any $c \geq c_{min}$, the profiles of the traveling waves were monotone decreasing or increasing. This minimum traveling wave speed can be obtained by direct computation in Expression (70) as

$$c_{min} = 2\sqrt{(1-\mu)(1-h(1-N_1)}. \tag{71}$$

Note that the computed eigenvalues lead directly to the cases stated in Lemma 1. The flow associated with the null eigenvalue is $\tilde{X}_1 = N_1$ and $\bar{X}_2 = 0$, as well as (by translation)

$\tilde{X}_1 = N_1$ and $\tilde{X}_2 = 1$. Hence, for $c < c_{min}$, a Hopf bifurcation occurs according to the form of the obtained eigenvalues.

Note that after computation of the corresponding flows by direct operations, the following leading terms are computed in the proximity of the critical point $\left(\tilde{X}_1, \tilde{Y}_1, \tilde{X}_2, \tilde{Y}_2\right) = \left(N_1, 0, 1, 0\right)$:

$$\tilde{X}_1 = C_1 e^{\lambda t}, \quad \tilde{X}_2 = C_2 e^{\lambda t}, \tag{72}$$

which shows the regular convergence of the traveling wave solutions in the proximity of the critical point. Note that $C_1 \in \mathbb{R}$, $C_2 \in \mathbb{R}$, and λ refer to each form of the eigenvalues obtained for the matrix detailed in (69). □

5.1. Application of the Singular Geometric Perturbation Theory

In this section, our intention was to use the singular geometric perturbation theory to define a perturbed manifold linked with (62), so that this theory can be employed to compute the traveling wave solutions. To this end, the following manifold was defined as follows:

$$\Omega_1 = \{\tilde{X}_1' = \tilde{Y}_1^{\frac{1}{p-1}}; \tilde{Y}_1' = -c\tilde{Y}_1^{\frac{1}{p-1}}\}, \tag{73}$$

in which the critical point $(N_2, 0, \mu, 0)$ holds.

Now, we define the perturbed manifold $\Omega_{1,\epsilon}$, which is considered in the proximity to Ω_1 :

$$\Omega_{1,\epsilon} = \{\tilde{X}_1 = N_2 - \epsilon; \tilde{X}_2 = \mu - \epsilon; \tilde{X}_1' = \tilde{Y}_1^{\frac{1}{p-1}}; \tilde{Y}_1' = -c\tilde{Y}_1^{\frac{1}{p-1}} + \left(1 - \mu + \epsilon\right)\left[h\tilde{X}_1 + (1-h)\tilde{X}_2\right]\epsilon\}. \tag{74}$$

Now, we have to show that Ω_1 is a normally hyperbolic manifold. To this end, we used the Fenichel invariant manifold theorem (refer to [30–32] for a complete description). As a first step, we shall show that the eigenvalues of the manifold Ω_1, specifically those whose eigenspaces are transversal to a tangential space (i.e., tangential to the the manifold), have a non zero real part. For this purpose, we consider a two-dimensional flow equivalent to Ω_1, which is given as

$$\begin{pmatrix} \tilde{X}_1' \\ \tilde{Y}_1' \end{pmatrix} = \begin{pmatrix} 0 & 1 \\ 0 & -c \end{pmatrix} \begin{pmatrix} \tilde{X}_1 \\ \tilde{Y}_1 \end{pmatrix}, \tag{75}$$

where, in the proximity of $\tilde{Y}_1 = 0$, we have considered that $\tilde{Y}_1^{\frac{1}{p-2}} \sim \tilde{Y}_1$. Even when the order of approach was different, the perturbation analysis was applied in the same manner as both functions $\tilde{Y}_1^{\frac{1}{p-2}}$ and $\tilde{Y}_1$ tend toward zero whenever $\tilde{Y}_1 \to 0^+$.

After solving the above expression, we firstly obtain the eigenvalues $(0, -c)$. Using the null eigenvalue, we obtain $(1, 0)$ as an eigenvector, which is tangent to the manifold Ω_1. As such, we can conclude that Ω_1 is a hyperbolic manifold as the only null real part eigenvalue leads to a tangential eigenvector.

Now, we have to show that $\Omega_{1,\epsilon}$ is locally invariant under the flow given by (62). For this purpose, with the help of [31], we state that, for all $r > 0$, there exists an open interval K with $c \in K$, and, for any value of $j \in K$, there exists a δ such that for $\epsilon \in (0, \delta)$, the manifold $\Omega_{1,\epsilon}$ is invariant. For $j > 0$, the following expression holds:

$$\begin{aligned} \tilde{\psi}_1 &= N_2 - \epsilon \\ \tilde{\psi}_2 &= 1 - \epsilon \\ \tilde{\psi}_3 &= -c\tilde{Y}_1^{\frac{1}{p-1}} \\ \tilde{\psi}_4 &= -c\tilde{Y}_1^{\frac{1}{p-1}} + \left(1 - \mu + \epsilon\right)\left[h\tilde{X}_1 + (1-h)\tilde{X}_2\right]\epsilon, \end{aligned} \tag{76}$$

where the above functions are $C^j\left(\bar{B}_r(0)\times(0,\delta)\right)$ and are sufficiently close to the equilibrium point $\left(N_2,0,\mu,0\right)$.

For any value of $r>0$, we can choose the set $\Omega_1\cap B_r(0)$ that is sufficiently large to control the whole traveling wave evolution. Note that δ is assessed with the distance between the defined flows under Ω_1 and $\Omega_{1,\epsilon}$. To this end, we admit that each function is measurable a.e. in $B_r(0)$. As such, we have the following:

$$\left\|\tilde{\psi}_4^{\Omega_1}-\tilde{\psi}_4^{\Omega_{1,\epsilon}}\right\|\leq\delta\epsilon. \tag{77}$$

According to the Fenichel invariant manifold theorem (again, refer to [30–32] for a complete description), the hyperbolic invariance condition is given for any $\delta\in(0,\infty)$. In this case, it is sufficient to consider

$$\delta=|1-\mu+\epsilon||hN_2+(1-h)\mu|. \tag{78}$$

Proceeding analogously, the following manifold Ω_2 is defined similarly as Ω_1 as follows:

$$\Omega_2=\{\tilde{X}_2'=\tilde{Y}_2^{\frac{1}{p-1}};\tilde{Y}_2'=-c\tilde{Y}_2^{\frac{1}{p-1}}\}. \tag{79}$$

In this case, in the proximity of the critical point $(N_2,0,\mu,0)$, the perturbed manifold $\Omega_{2,\epsilon}$, which is close to Ω_1, is defined as follows:

$$\Omega_{2,\epsilon}=\{\tilde{X}_1=N_2-\epsilon;\tilde{X}_2=1-\epsilon;\tilde{X}_2'=\tilde{Y}_2^{\frac{1}{p-1}};\tilde{Y}_2'=-c\tilde{Y}_2^{\frac{1}{p-1}}+\left(1-\mu+\epsilon\right)\left[h\tilde{X}_1+(1-h)\tilde{X}_2\right]\epsilon\}. \tag{80}$$

Similar to how was performed for Ω_1, we made use of the Fenichel invariant manifold theorem. For this purpose, we considered a reduced two-dimensional flow equivalent to Ω_2, which was given as follows:

$$\begin{pmatrix}\tilde{X}_2'\\ \tilde{Y}_2'\end{pmatrix}=\begin{pmatrix}0 & 1\\ 0 & -c\end{pmatrix}\begin{pmatrix}\tilde{X}_2\\ \tilde{Y}_2\end{pmatrix}, \tag{81}$$

where $(0,-c)$ are the eigenvalues of the above expression, which shows that they were real and that one is null. The eigenvector corresponding the to zero real part eigenvalue was tangential (i.e., not transversal) to Ω_2.

Following this, our intention was to show that $\Omega_{2,\epsilon}$ is locally invariant under the flow given by (62). For this purpose, the following expression holds:

$$\begin{aligned}\tilde{\psi}_1' &= N_2-\epsilon\\ \tilde{\psi}_2' &= \mu-\epsilon\\ \tilde{\psi}_3' &= -c\tilde{Y}_2^{\frac{1}{p-1}}\\ \tilde{\psi}_4' &= -c\tilde{Y}_2^{\frac{1}{p-1}}+\left(1-\mu+\epsilon\right)\left[h\tilde{X}_1+(1-h)\tilde{X}_2\right]\epsilon.\end{aligned} \tag{82}$$

Note that the above functions are $C^j\left(B_r\bar{(}0)\times(0,\delta)\right)$ in the proximity of the equilibrium point $\left(N_2,0,\mu,0\right)$.

In the same manner, δ is assessed in the assumption that the functions in (82) are measurable a.e $B_r(0)$. As such, we have the following:

$$\left\|\tilde{\psi}_4'^{\Omega_2}-\tilde{\psi}_4'^{\Omega_{2,\epsilon}}\right\|\leq\delta\epsilon, \tag{83}$$

where δ is defined as per the Fenichel conditions that were already assessed in (78).

In this section, it has been shown that both the two-dimensional manifolds Ω_1 and Ω_2 remained invariant under the flow given in (62). Consequently, the asymptotic profiles of the traveling waves can be obtained by considering the dimensionally reduced Ω_1 and Ω_2 or the asymptotic ones of $\Omega_{1,\epsilon}$ and $\Omega_{2,\epsilon}$.

To make a clear traceability of the assessments to come, we considered the following manifolds in the proximity of the critical point $(N_1, 0, 1, 0)$:

$$\tilde{\Omega}_1 = \{\tilde{X}_1' = \tilde{Y}_1^{\frac{1}{p-1}}; \tilde{Y}_1' = -c\tilde{Y}_1^{\frac{1}{p-1}}\} \tag{84}$$

and

$$\tilde{\Omega}_2 = \{\tilde{X}_2' = \tilde{Y}_2^{\frac{1}{p-1}}; \tilde{Y}_2' = -c\tilde{Y}_2^{\frac{1}{p-1}}\}, \tag{85}$$

where the perturbed manifold $\tilde{\Omega}_{1,\epsilon}$ and $\tilde{\Omega}_{2,\epsilon}$ in the proximity of $\tilde{\Omega}_1$ and $\tilde{\Omega}_2$ are, respectively, the following:

$$\tilde{\Omega}_{2,\epsilon} = \{\tilde{X}_1 = N_1 - \epsilon; \tilde{X}_2 = 1 - \epsilon; \tilde{X}_1' = \tilde{Y}_1^{\frac{1}{p-1}}; \tilde{Y}_1' = -c\tilde{Y}_1^{\frac{1}{p-1}} - (1 - \mu - \epsilon)\Big[h\tilde{X}_1 + (1-h)\tilde{X}_2\Big]\epsilon\} \tag{86}$$

and

$$\tilde{\Omega}_{2,\epsilon} = \{\tilde{X}_1 = N_1 - \epsilon; \tilde{X}_2 = 1 - \epsilon; \tilde{X}_2' = \tilde{Y}_2^{\frac{1}{p-1}}; \tilde{Y}_2' = -c\tilde{Y}_2^{\frac{1}{p-1}} - (1 - \mu - \epsilon)\Big[h\tilde{X}_1 + (1-h)\tilde{X}_2\Big]\epsilon\}. \tag{87}$$

When applying a similar procedure as we developed for the critical point $(N_2, 0, \mu, 0)$, we can show that $\tilde{\Omega}_1$, $\tilde{\Omega}_2$, $\tilde{\Omega}_{1,\epsilon}$, and $\tilde{\Omega}_{2,\epsilon}$ are normally hyperbolic manifolds. Also, we can show that these two manifolds are locally invariant under the flow given by (62).

5.2. Finite Propagation and Profiles

Consider the perturbed manifold $\Omega_{1,\epsilon}$ having the following family of trajectories in the phase plane $(\tilde{X}_1, \tilde{Y}_1)$:

$$\frac{d\tilde{Y}_1}{d\tilde{X}_1} = -c + (1 - \mu + \epsilon)\Big[h\tilde{X}_1 + (1-h)\tilde{X}_2\Big]\epsilon\tilde{Y}_1^{-\frac{1}{p-1}} = H\Big(\tilde{X}_1, \tilde{X}_2, \tilde{Y}_1\Big), \tag{88}$$

$0 < \tilde{X}_1 < N_2$, $0 < \tilde{X}_1 < \mu$, $\tilde{Y}_1 > 0$.

To show that a regular trajectory in the phase space $(\tilde{X}_1, \tilde{Y}_1)$ exists, we shall consider the condition $h(1 - N_2) \geq \mu$, which was pointed out in Lemma 1.

Note that, under condition $h(1 - N_2) \geq \mu$, the following holds:

$$(1 - \mu + \epsilon)\Big[h\tilde{X}_1 + (1-h)\tilde{X}_2\Big]\epsilon \leq 0. \tag{89}$$

For $c \to 0$, then $\frac{d\tilde{Y}_1}{d\tilde{X}_1} < 0$, while for increasing values of c and sufficiently small values of ϵ, close the critical point; as such, we have $\frac{d\tilde{Y}_1}{d\tilde{X}_1} > 0$. In addition, we remark that the function $H(\tilde{X}_1, \tilde{Y}_1)$ is continuous in its domain. Based on this topological arguments, we state that there exists a regular trajectory close the critical point in the phase plane $(\tilde{X}_1, \tilde{Y}_1)$, which is given by the following:

$$-c + (1 - \mu + \epsilon)\Big[h\tilde{X}_1 + (1-h)\tilde{X}_2\Big]\epsilon\tilde{Y}_1^{-\frac{1}{p-1}} = H\Big(\tilde{X}_1, \tilde{X}_2, \tilde{Y}_1\Big) = 0. \tag{90}$$

In the proximity of $\tilde{X}_2 = \mu$, the following trajectory holds

$$c\tilde{Y}_1^{\frac{1}{p-1}} - h(1 - \mu + \epsilon)\tilde{X}_1\epsilon = (1-h)(1 - \mu + \epsilon)\mu\epsilon. \tag{91}$$

Note that a particular traveling wave profile is obtained considering the density and flux functions introduced in (61)

$$\tilde{F}_1'(\zeta) - \frac{h\epsilon(1-\mu+\epsilon)}{c}\tilde{F}_1(\zeta) = \frac{(1-h)(1-\mu+\epsilon)\mu\epsilon}{c}. \tag{92}$$

After solving (92), we have

$$\tilde{F}_1(\zeta) = -\frac{(1-h)\mu}{h} + A_{13}e^{\frac{h\epsilon(1-\mu+\epsilon)}{c}\zeta}. \tag{93}$$

Since ϵ shall be small, as mentioned in the perturbed manifold, so we shall consider that $\epsilon\zeta << 1$. For this, it suffices to consider an epsilon law of the form $\epsilon(\zeta) = e^{-\zeta^2}$. After applying the condition $\tilde{F}_1(\infty) = N_1$, we have $A_{13} \sim N_2 + \frac{(1-h)\mu}{h}$, so Expression (93) becomes

$$\tilde{F}_1(\zeta) = -\frac{(1-h)\mu}{h} + \left(N_2 + \frac{(1-h)\mu}{h}\right)e^{\frac{h\epsilon(1-\mu+\epsilon)}{c}\zeta}. \tag{94}$$

Once a profile has been obtained for $\tilde{F}_1$, a similar process shall be repeated for manifold $\Omega_{2,\epsilon}$ in the phase plane $(\tilde{X}_2, \tilde{Y}_2)$. Note that such a process is similar to that which was already described in the phase plane $(\tilde{X}_1, \tilde{Y}_1)$. For the sake of simplicity, and by considering the density and flux variables in (61), the trajectory is given by the following:

$$\tilde{F}_2'(\zeta) - \frac{(1-h)(1-\mu+\epsilon)\epsilon}{c}\tilde{F}_2(\zeta) = \frac{hN_2\epsilon(1-\mu+\epsilon)}{c}. \tag{95}$$

After solving (95), we have

$$\tilde{F}_2(\zeta) = -\frac{hN_2}{1-h} + A_{14}e^{\frac{(1-h)(1-\mu+\epsilon)\epsilon}{c}\zeta}. \tag{96}$$

After using $\tilde{F}_2(\infty) = \mu$, we obtain $A_{14} \sim \mu + \frac{hN_2}{1-h}$, so Expression (96) becomes

$$\tilde{F}_2(\zeta) = -\frac{hN_2}{1-h} + \left(\mu + \frac{hN_2}{1-h}\right)e^{\frac{(1-h)(1-\mu+\epsilon)\epsilon}{c}\zeta}. \tag{97}$$

Now, consider the perturbed manifold $\tilde{\Omega}_{1,\epsilon}$ as having the following family of trajectories in the phase plane $(\tilde{X}_1, \tilde{Y}_1)$:

$$\frac{d\tilde{Y}_1}{d\tilde{X}_1} = -c - (1-\mu-\epsilon)\left[h\tilde{X}_1 + (1-h)\tilde{X}_2\right]\epsilon\tilde{Y}_1^{-\frac{1}{p-1}} = H\left(\tilde{X}_1, \tilde{X}_2, \tilde{Y}_1\right), \tag{98}$$

$0 < \tilde{X}_1 < N_1, 0 < \tilde{X}_1 < 1, \tilde{Y}_1 > 0$.

To show that a regular trajectory in the phase plane $(\tilde{X}_1, \tilde{Y}_1)$ exists, we considered condition $h(1-N_1) \leq 1$, as pointed out in Lemma 1.

Note that, under condition $h(1-N_1) \leq 1$, the following holds:

$$\left[hX_1 + (1-h)X_2\right]\epsilon \geq 0. \tag{99}$$

For $c \to 0$, then $\frac{dY_1}{dX_1} < 0$, while for increasing values of c and sufficiently small values of ϵ, we close the critical point as $\frac{dY_1}{dX_1} > 0$. Function $H(X_1, Y_1)$ is continuous in its domain. Based on this topological argument, there exists a regular trajectory that is close to the critical point in the phase plane (X_1, Y_1), which is given by the following:

$$-c-(1-\mu-\epsilon)\left[h\tilde{X}_1+(1-h)\tilde{X}_2\right]\epsilon\tilde{Y}_1^{-\frac{1}{p-1}}=H\left(\tilde{X}_1,\tilde{X}_2,\tilde{Y}_1\right)=0. \tag{100}$$

In the proximity of $\tilde{X}_2=1$, the following trajectory holds

$$c\tilde{Y}_1^{\frac{1}{p-1}}+h(1-\mu-\epsilon)\tilde{X}_1\epsilon=-(1-h)(1-\mu-\epsilon)\epsilon. \tag{101}$$

Note that a particular traveling wave profile is obtained by considering the density and flux function introduced in (61) as follows:

$$\tilde{F}_1'(\zeta)+\frac{h\epsilon(1-\mu-\epsilon)}{c}\tilde{F}_1(\zeta)=-\frac{(1-h)(1-\mu-\epsilon)\epsilon}{c}. \tag{102}$$

After solving (102), we have

$$\tilde{F}_1(\zeta)=-\frac{(1-h)}{h}+A_{15}e^{-\frac{h\epsilon(1-\mu-\epsilon)}{c}\zeta}, \tag{103}$$

where A_{15} shall be assessed by considering $\tilde{F}_1(\infty)=N_1$. Then, the above expression can be written as follows:

$$\tilde{F}_1(\zeta)=-\frac{(1-h)}{h}+\left(N_1+\frac{(1-h)}{h}\right)e^{-\frac{h\epsilon(1-\mu-\epsilon)}{c}\zeta}. \tag{104}$$

Once a profile has been obtained for $\tilde{F}_1$, a similar process shall be repeated for the manifold $\tilde{\Omega}_{2,\epsilon}$ in the phase plane $(\tilde{X}_2,\tilde{Y}_2)$. Note that such a process is similar to that which was already described for plane $(\tilde{X}_2,\tilde{Y}_2)$. For the sake of simplicity, as well as by considering the density and flux variables in (61), the trajectory is given by the following:

$$\tilde{F}_2'(\zeta)+\frac{(1-h)(1-\mu-\epsilon)\epsilon}{c}\tilde{F}_2(\zeta)=-\frac{hN_1\epsilon(1-\mu-\epsilon)}{c}. \tag{105}$$

After solving (105), we have

$$\tilde{F}_2(\zeta)=-\frac{hN_1}{1-h}+A_{16}e^{-\frac{(1-h)(1-\mu-\epsilon)\epsilon}{c}\zeta}. \tag{106}$$

After using $\tilde{F}_2(\infty)=1$, then the above expression can be written as

$$\tilde{F}_2(\zeta)=-\frac{hN_1}{1-h}+\left(1+\frac{hN_1}{1-h}\right)e^{-\frac{(1-h)(1-\mu-\epsilon)\epsilon}{c}\zeta}. \tag{107}$$

5.3. Numerical Assessment and Comparison with Analytical Profiles

Our target now is to introduce a numerical resolution of System (62) so that we can compare with the analytical forms obtained after the application of the geometric perturbation theory. This section is mainly devoted to the introduction of a validation of the different hypotheses performed in Sections 4.1 and 4.2. Hence, our numerical assessment does not have the objective of building technical discussions that are related with real scenarios of flame propagation. In actuality, such applied scenarios are not provided here, which constitutes a limitation in our work. We hope that our analytical assessments (which are further supported by the numerical expressions detailed hereafter) will lead to additional studies in applied fields.

For the numerical assessment, we focused only on the critical point $(N_2, 0, \mu, 0)$, where N_2 is given in Expression (65). It should be mentioned that we conducted similar assessments for the other critical point $(N_1, 0, 1, 0)$ with similar results. Hence, due to desiring a concise discussion, we will consider the mentioned point $(N_2, 0, \mu, 0)$.

First, it is relevant to provide practical values for the constants involved in Model (62). We will consider that the traveling waves speed, c, may change, thus leading to different profiles of solutions. The following specific values were assumed:

$$h = 0.4;\ \epsilon = 0.01;\ \mu = 0.6;\ p = 3. \tag{108}$$

Given these fixed constants, and for each value in the traveling wave speed, we can determine N_2, as per (65), to obtain a specific value for the critical point $(N_2, 0, \mu, 0)$.

The numerical assessment was supported by the MATLAB function *bvp4c* (see [33] for a detailed description). The initial data were introduced as a step distribution, and we looked for the heteroclinic connection between the critical point $(N_2, 0, \mu, 0)$ and a flame relaxed condition (the profiles of solutions tended toward null at $\zeta \to \infty$). This approximation was physically plausible as we may assume that the propagation of the flame, before relaxing, is stationary and around the critical point $(N_2, 0, \mu, 0)$. Then, the question to answer is about the evolution of the flame from such a critical state to the relaxation condition, and this was considered to occur for $\zeta > 0$. The main question here is related with the exponential forms of the propagating tail while evolving in $\zeta > 0$.

The domain of integration was considered to be large to ensure the relaxation condition in the flame; as such, it was set as $D = 10,000$. In addition, such a domain is relevant for avoiding the influence of the collocation method, which is used by the *bvp4c* routine. The number of nodes was considered to be 100,000, and the required global error level was 10^{-4}. It is important to highlight that, in all the cases executed under these principles, the error level was achieved.

The results of the numerical analysis and each of the comparison arguments are given in Figures 2–6. It is relevant to note that the numerical solutions were obtained from the *bvp4c* application to Problem (62), while the analytical solutions obtained were due to the application of the geometric perturbation theory (called *gpt* in each figure), which is given in Expressions (94) and (97).

As it can be inferred, the traveling wave was assumed as common for both solutions. The forms of the solutions were provided in accordance with different values in the traveling wave speed. These presented results led us to state on the validity of the hypothesis conducted in the construction of traveling wave profiles that are based on the geometric perturbation theory.

Once we observe that the analytical solutions (see the red line in Figures 1–3) trespass the numerical ones while increasing the traveling speed, we can infer that there exists an optimal traveling wave speed, c_{opt}, for which both the numerical and the *gpt* solutions are close and evolve similarly in accordance with an exponential law (which is predicted by Solutions (94) and (97)). We have performed a numerical exploration for finding such optimal value, thereby leading to $c_{opt} = 0.701$ for a global error (or distance) between the numerical and the *gpt* solutions in (94) and (97) for a maximum of 10^{-3}.

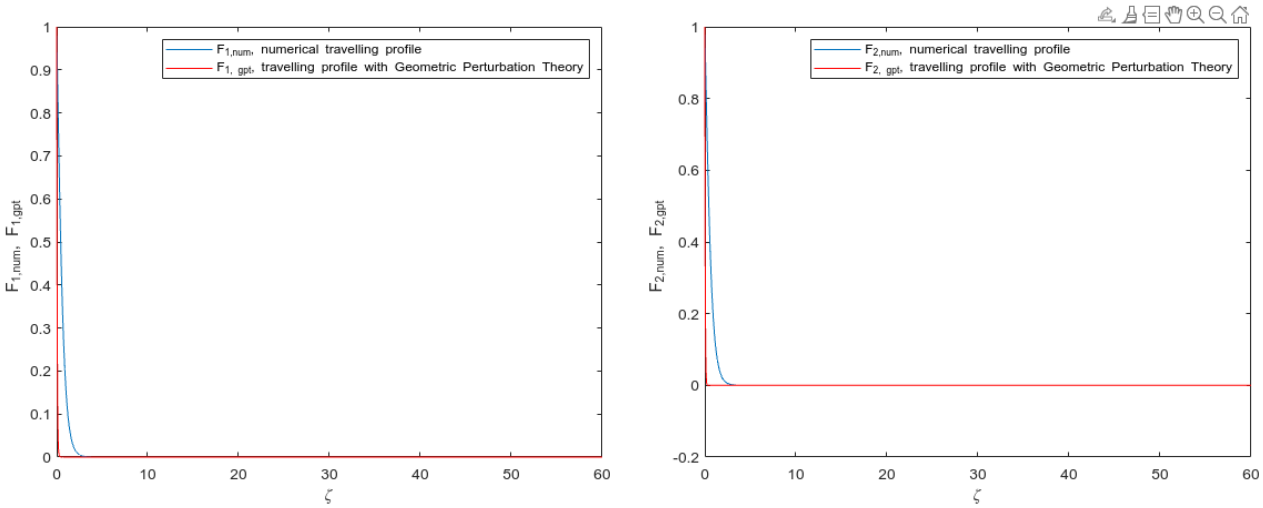

Figure 2. Representation of the solutions for $c = 0.1$. The figure on the left refers to Solution F_1 (linked with $\tilde{u}$), while the figure on the right provides the form of the Solution F_2 (linked with $\tilde{v}$). It is interesting to observe that the decaying rate in the numerical solution (blue) may fit with the exponential behavior obtained in the analytical solution (red), but we should continue exploring with other traveling wave speeds to confirm this statement accurately.

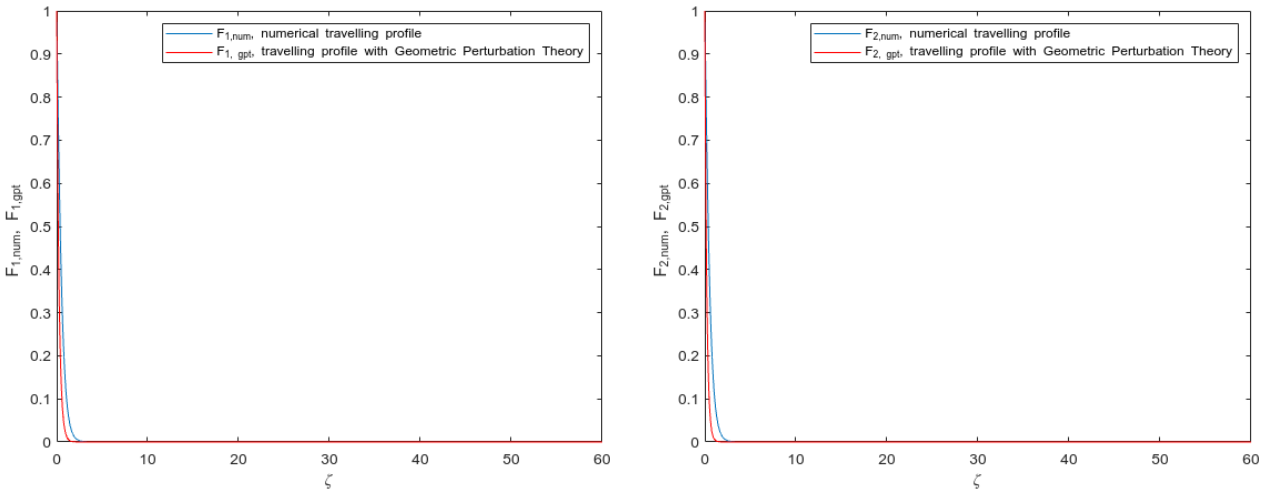

Figure 3. Representation of the solutions for $c = 0.5$. The figure on the left refers to Solution F_1 (linked with $\tilde{u}$), while the figure on the right provides the form of Solution F_2 (linked with $\tilde{v}$). It is interesting to observe that the exponential relaxation condition holds for both solutions and that both the numerical and *gpt* solutions are very close upon evolution. We state that increasing the traveling wave speed has a positive effect, as the analytical solutions (94) and (97) evolved in a very similar fashion to the numerical solutions.

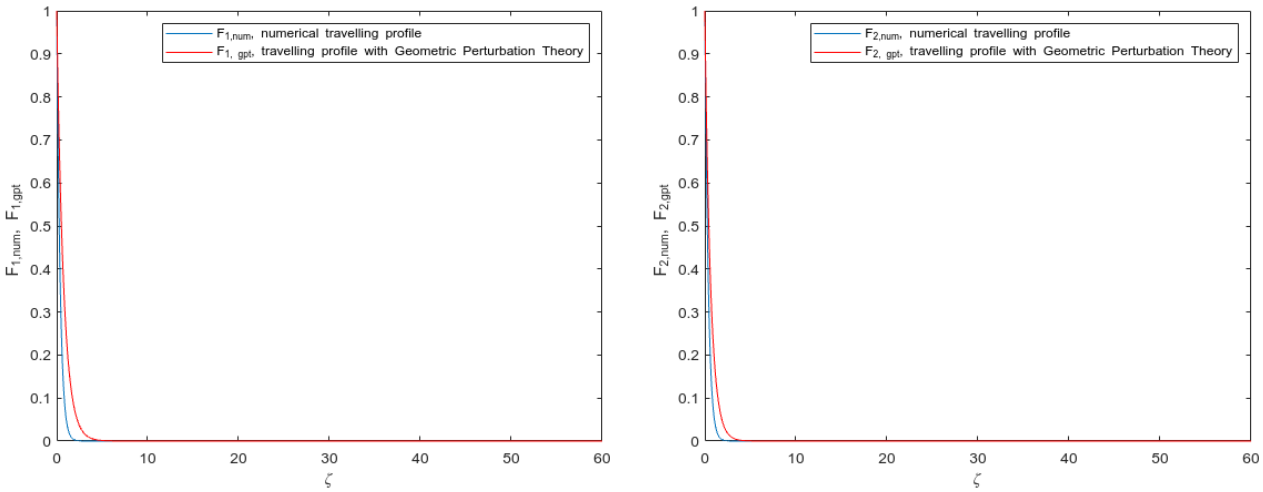

Figure 4. Representation of the solutions for $c = 1.5$. The up figure refers to Solution F_1 (linked with $\tilde{u}$), while the down figure provides the form of Solution F_2 (linked with $\tilde{v}$). It is interesting to observe that the exponential relaxation condition holds for both solutions and that both the numerical and *gpt* solutions increase their distances when the traveling wave speed increases. One should note that the *gpt* solution (red) is above the numerical solution (blue). This fact suggests the existence of an optimal traveling wave speed, such that the error between both solutions is minimal. We can infer this by a direct observation of Figures 1 and 2 (where the *gpt* solutions were under the numerical ones), which were unlike the case where $c = 1.5$.

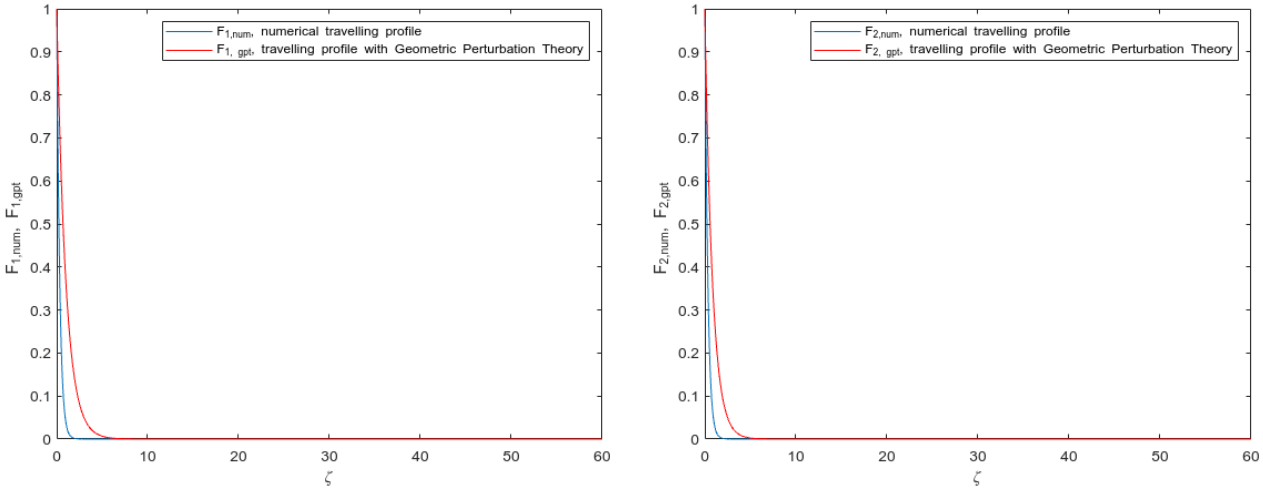

Figure 5. Representation of the solutions for $c = 2$. The figure on the left refers to Solution F_1 (linked with $\tilde{u}$), while the figure on the right provides the form of Solution F_2 (linked with $\tilde{v}$). Both solutions increase their distances when increasing the traveling wave speed.

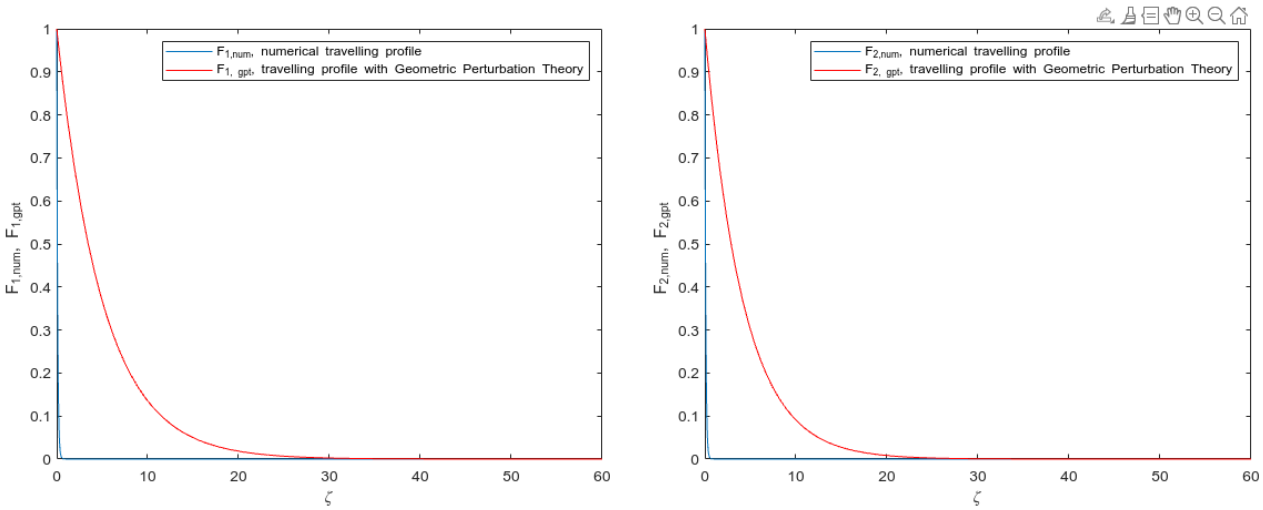

Figure 6. Representation of the solutions for $c = 10$. The figure on the left refers to Solution F_1 (linked with $\tilde{u}$), while the figure on the right provides the form of Solution F_2 (linked with $\tilde{v}$). Again, both solutions increase their distances when increasing the traveling wave speed. This fact reflects either that the traveling speed may not be fully representative of a physical scenario or that our analytical solution fails at higher traveling speeds. Additional real tests would be required to further support these statements.

6. Profiles of Analytical Solutions

The objective in this section is to continue the exploration on the behavior of solutions to (4)–(6). The analysis starts with the searching of analytical upper solutions. We departed from the Systems (4)–(6), and we applied the following ideas in the search of upper bounding terms as follows:

$$\frac{\partial \tilde{u}}{\partial t} \leq \frac{\partial}{\partial y}\left(\left(\frac{\partial \tilde{u}}{\partial y}\right)^{p-2}\frac{\partial \tilde{u}}{\partial y}\right) + h(1+\mu)\tilde{u}\tilde{v} + (1+\mu)v^2 \tag{109}$$

and

$$\frac{\partial \tilde{v}}{\partial t} \leq \frac{\partial}{\partial y}\left(\left(\frac{\partial \tilde{v}}{\partial y}\right)^{p-2}\frac{\partial \tilde{u}}{\partial y}\right) + h(1+\mu)\tilde{u}\tilde{v} + (1+\mu)v^2. \tag{110}$$

Consequently, a supersolution can be obtained from the following governing equation:

$$\frac{\partial \tilde{u}}{\partial t} = \frac{\partial}{\partial y}\left(\left(\frac{\partial \tilde{u}}{\partial y}\right)^{p-2}\frac{\partial \tilde{u}}{\partial y}\right) + h(1+\mu)\tilde{u}\tilde{v} + (1+\mu)v^2 \tag{111}$$

and

$$\frac{\partial \tilde{v}}{\partial t} = \frac{\partial}{\partial y}\left(\left(\frac{\partial \tilde{v}}{\partial y}\right)^{p-2}\frac{\partial \tilde{u}}{\partial y}\right) + h(1+\mu)\tilde{u}\tilde{v} + (1+\mu)v^2. \tag{112}$$

The exploration of solutions was performed based on self-similar structures of the following form:

$$\tilde{u}(y,t) = t^{-\gamma_1}\tilde{f}(\zeta), \quad \zeta = |y|t^{\gamma_2} \tag{113}$$

and

$$\tilde{v}(y,t) = t^{-\gamma_3}\tilde{g}(\zeta), \quad \zeta = |y|t^{\gamma_4}. \tag{114}$$

After replacing Expressions (113) and (114) into (111) and (112), respectively, we obtained

$$\begin{aligned} -\gamma_1 t^{-\gamma_1-1}\tilde{f} &+ \gamma_2 t^{-\gamma_1-1}\zeta\tilde{f}' = (p-1)t^{-\gamma_1(p-1)+\gamma_2}\left(\tilde{f}'\right)^{p-2}\tilde{f}'' \\ &+ h(1+\mu)t^{-(\gamma_1+\gamma_3)}\tilde{f}\tilde{g} + (1+\mu)t^{-2\gamma_3}\tilde{g}^2 \end{aligned} \tag{115}$$

and

$$\begin{aligned} -\gamma_3 t^{-\gamma_3-1}\tilde{f} &+ \gamma_4 t^{-\gamma_3-1}\zeta\tilde{f}' = (p-1)t^{-\gamma_3(p-1)+\gamma_4}\left(\tilde{f}'\right)^{p-2}\tilde{f}'' \\ &+ h(1+\mu)t^{-(\gamma_1+\gamma_3)}\tilde{f}\tilde{g} + (1+\mu)t^{-2\gamma_3}\tilde{g}^2. \end{aligned} \tag{116}$$

By equating the powers of t in the given equations and solving them, we obtained the values for γ_1, γ_2, γ_3, and γ_4 as follows:

$$\begin{aligned} \gamma_1 &= \frac{\gamma_2}{p-2} + \frac{1}{p-2}, \\ \gamma_3 &= 1, \\ \gamma_4 &= p-3. \end{aligned}$$

These expressions indicates the relationships between the parameters γ_1, γ_2, γ_3, γ_4, and p, where γ_1 and γ_4 were expressed in terms of γ_2 and p. This symbolic resolution helped to elucidate the interdependencies among these parameters within the framework of the self-similar solutions.

The asymptotic solutions to (115) and (116) can be obtained at each selected time (for simplification and without loss of generality, we consider that t = 1) by solving the following equations:

$$(p-1)\left(\tilde{f}'\right)^{p-2}\tilde{f}'' - \gamma_2\zeta\tilde{f}' + \gamma_1\tilde{f} + h(1+\mu)\tilde{f}\tilde{g} + (1+\mu)\tilde{g}^2 = 0 \tag{117}$$

and

$$(p-1)\left(\tilde{g}'\right)^{p-2}\tilde{g}'' - \gamma_4\zeta\tilde{g}' + \gamma_3\tilde{g} + h(1+\mu)\tilde{f}\tilde{g} + (1+\mu)\tilde{g}^2 = 0. \tag{118}$$

When subtracting (118) from (117), we have

$$\frac{d}{d\zeta}\left(\tilde{f}'\right)^{p-1} - \gamma_2\frac{d}{d\zeta}(\zeta\tilde{f}) - \left[\frac{d}{d\zeta}\left(\tilde{g}'\right)^{p-1} - \gamma_4\frac{d}{d\zeta}(\zeta\tilde{g})\right] = 0, \tag{119}$$

where $\gamma_2 = -\gamma_1$. By integrating (119), we have

$$\left(\tilde{f}'\right)^{p-1} - \gamma_2(\zeta\tilde{f}) - \left[\left(\tilde{g}'\right)^{p-1} - \gamma_4(\zeta\tilde{g})\right] = A_{17}. \tag{120}$$

Under an asymptotic condition, we can assume that the flame relaxes. Then, for $\zeta \to \infty$: $\tilde{f} \to 0$ and $\tilde{g} \to 0$, we hence take $A_{17} = 0$; as such, the above equation becomes

$$\left(\tilde{f}'\right)^{p-1} - \gamma_2(\zeta\tilde{f}) - \left[\left(\tilde{g}'\right)^{p-1} - \gamma_4(\zeta\tilde{g})\right] = 0, \tag{121}$$

where one possibility is

$$\left(\tilde{f}'\right)^{p-1} - \gamma_2(\zeta\tilde{f}) = 0 \tag{122}$$

and

$$\left(\tilde{g}'\right)^{p-1} - \gamma_4(\zeta\tilde{g}) = 0. \tag{123}$$

After solving (122) and (123), we obtain

$$\tilde{f}(\zeta) = \frac{\gamma_2^{\frac{1}{p-2}}(p-2)^{\frac{p-1}{p-2}}}{p^{\frac{p-1}{p-2}}}\zeta^{\frac{p}{p-2}} \tag{124}$$

and

$$\tilde{g}(\zeta) = \frac{\gamma_4^{\frac{1}{p-2}}(p-2)^{\frac{p-1}{p-2}}}{p^{\frac{p-1}{p-2}}}\zeta^{\frac{p}{p-2}}. \tag{125}$$

By putting (124) and (125) into (113) and (114), we have

$$\tilde{u}(y,t) = t^{-\gamma_1}\frac{\gamma_2^{\frac{1}{p-2}}(p-2)^{\frac{p-1}{p-2}}}{p^{\frac{p-1}{p-2}}}(yt^{\gamma_2})^{\frac{p}{p-2}} \tag{126}$$

and

$$\tilde{v}(y,t) = t^{-\gamma_3}\frac{\gamma_4^{\frac{1}{p-2}}(p-2)^{\frac{p-1}{p-2}}}{p^{\frac{p-1}{p-2}}}(yt^{\gamma_4})^{\frac{p}{p-2}}. \tag{127}$$

Note that Figures 7 and 8 provide representations of the self-similar solutions in Sections (126) and (127). The figures represent self-similar solutions to the problem that involves $\tilde{u}(y,t)$ and $\tilde{v}(y,t)$, which are integral to understanding the dynamics of flame evolution. Self-similar solutions, which are characterized by their invariance under scaling transformations, are particularly apt for problems where phenomena exhibit scaling behavior, as often observed in flame propagation and diffusion processes. The solutions $\tilde{u}(y,t)$ and $\tilde{v}(y,t)$ take the form of the scaling functions of $\zeta = |y|t^{\gamma_i}$, thus exemplifying this property.

The plots revealed a detailed structure of the flame, where the peak intensities and variations were not confined to a single central peak as would be seen in a bell-shaped curve. Instead, they displayed a rather more varied distribution. This is indicative of multiple zones of high intensity within the flame in the porous domain, which are characterized by the values of p.

Note that in Figures 9 and 10, the considered value of $\gamma_2 = -2$. In the analysis of the 3D plots for $\tilde{u}(y,t)$ and $\tilde{v}(y,t)$ with $\gamma_2 = 1$ and $\gamma_2 = -2$, we observed that the spatial distribution and temporal evolution of the solutions with $\gamma_2 = -2$ showed more localized peaks and varied changes, thus contrasting with the relative uniformity observed for when $\gamma_2 = 1$. These differences underscore the sensitivity of flame modeling to the γ_2 parameter. It seems as though a positive γ_2 represents typical smooth flame propagation environments, while a negative γ_2 suggests a departure from standard dynamics, thus pointing toward complex physical phenomena within the flame. Understanding the influence of γ_2 is crucial for developing predictive models that can accurately capture the nuances of different combustion scenarios, which can range from controlled settings to turbulent, natural environments. Based on our findings, the γ_2 parameter plays a relevant role in solution geometries. Certainly, experimental setups are required to further explore flame behavior and its connection with the γ_2 parameter. This experimental setup often involves the use of semi-empirical models. These models are typically derived for specific types of fires, such as surface fuels or pool fires. For instance, in the case of wildland fires, semi-empirical models have been applied to understand flame geometry, which is crucial for predicting fire behavior. Such models involve assessing the flame's tilt, height, and length, as well as comparing these with experimental observations, which often lead to the development of power–law correlations. These correlations can then be used to derive coefficients for

models through regression analysis. This approach has been successfully applied in studies of chaparral crown fires, thus demonstrating the applicability of semi-empirical models in diverse fire scenarios [34].

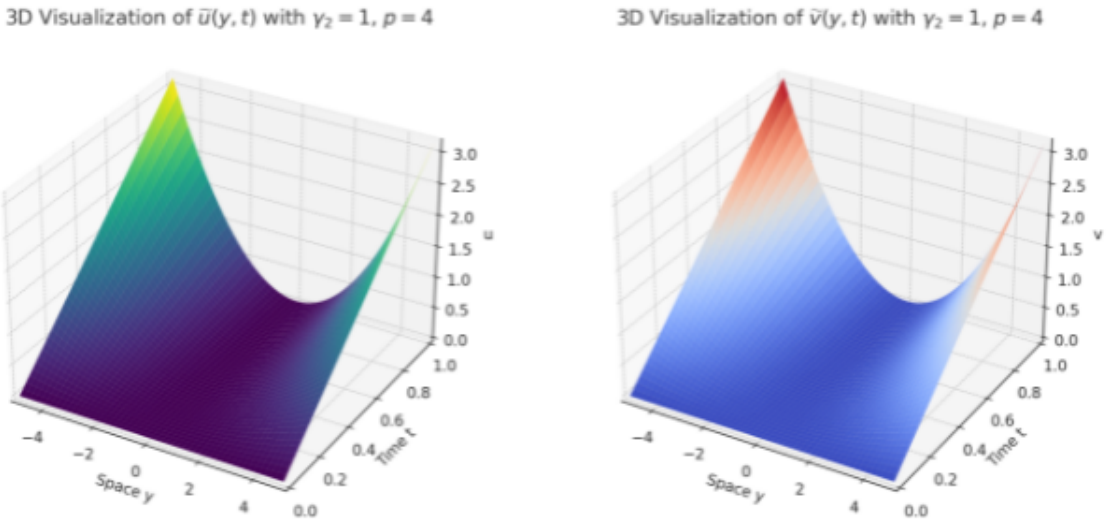

Figure 7. (**Left**): A 3D visualization of $\widetilde{u}(y,t)$ with the parameters $\gamma_2 = 1$ and $p = 4$. This plot illustrates the spatial–temporal evolution of the solution $\widetilde{u}$ on the z-axis, which extended over the space range and time up to $t = 1$. (**Right**): A 3D visualization of $\widetilde{v}(y,t)$ under the same parameters. This similarly depicts the behavior of $\widetilde{v}$, thus providing a comprehensive view of the solution's dynamics over space and time. Both of the plots capture the essence of flame dynamics, which are represented by these self-similar solutions. However, we recall that the represented functions do not directly provide the pressure and temperature values of the flame. To obtain the pressure and temperature values, the reader is referred to the linear transformations in Equation (2) of [3].

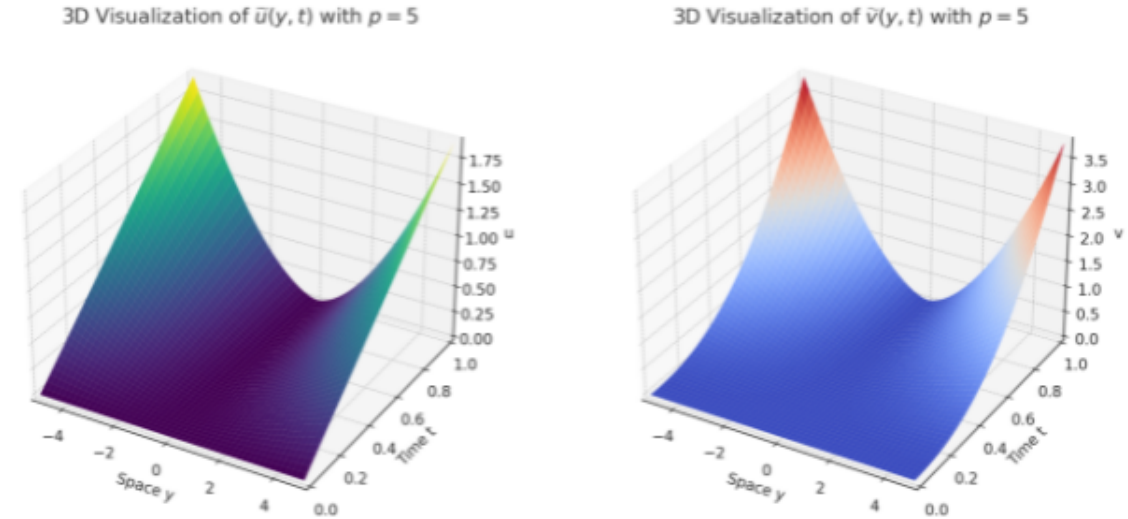

Figure 8. (**Left**): A 3D visualization of $\widetilde{u}(y,t)$ with the parameters $\gamma_2 = 1$ and $p = 5$. This plot illustrates the spatial–temporal evolution of the solution $\widetilde{u}$ on the z-axis, which extends over the space range and time up to $t = 1$. (**Right**): A 3D visualization of $\widetilde{v}(y,t)$ under the same parameters. This similarly depicts the behavior of $\widetilde{v}$, thereby providing a comprehensive view of the solution's dynamics over space and time. Both of the plots capture the essence of flame dynamics, which are represented by these self-similar solutions. To obtain the pressure and temperature values, the reader is referred to the linear transformations in Equation (2) of [3].

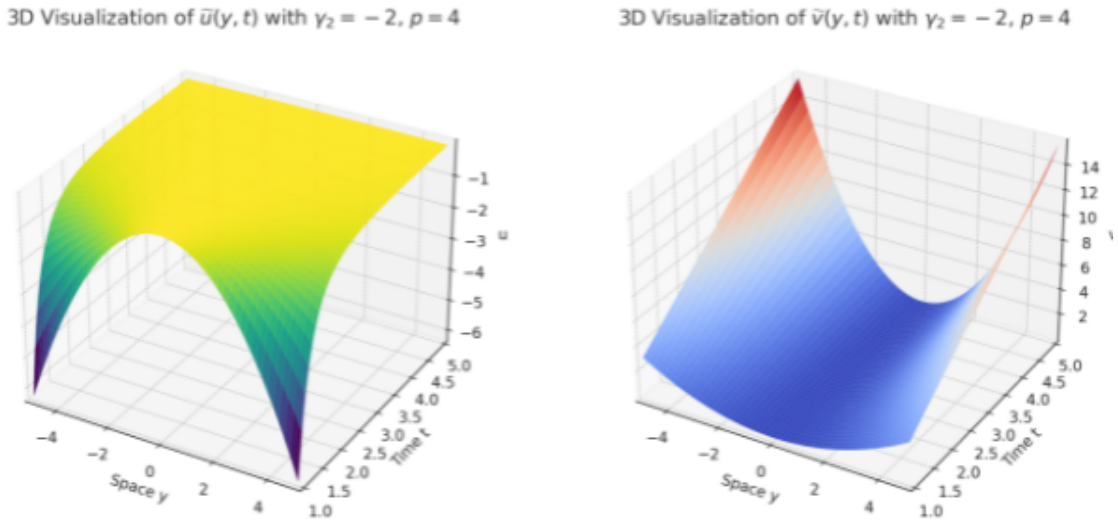

Figure 9. (**Left**): A 3D visualization of $\widetilde{u}(y,t)$ with the parameters $\gamma_2 = -2$ and $p = 4$. The plot illustrates the behavior of $\widetilde{u}$ over the spatial domain from $-L$ to L and time from 1 to 5, thus avoiding division by zero issues. (**Right**): A 3D visualization of $\widetilde{v}(y,t)$ under the same parameters. This plot similarly depicts the evolution of $\widetilde{v}$, thereby offering insights into its dynamics over the adjusted time and space range. Both plots demonstrate the complex behavior of the solutions, and these are influenced by the specific choices of γ_2 and p, thereby providing a nuanced view of the flame dynamics as described by self-similar solutions. Again, to obtain the pressure and temperature values, the reader is referred to the linear transformations in Equation (2) of [3].

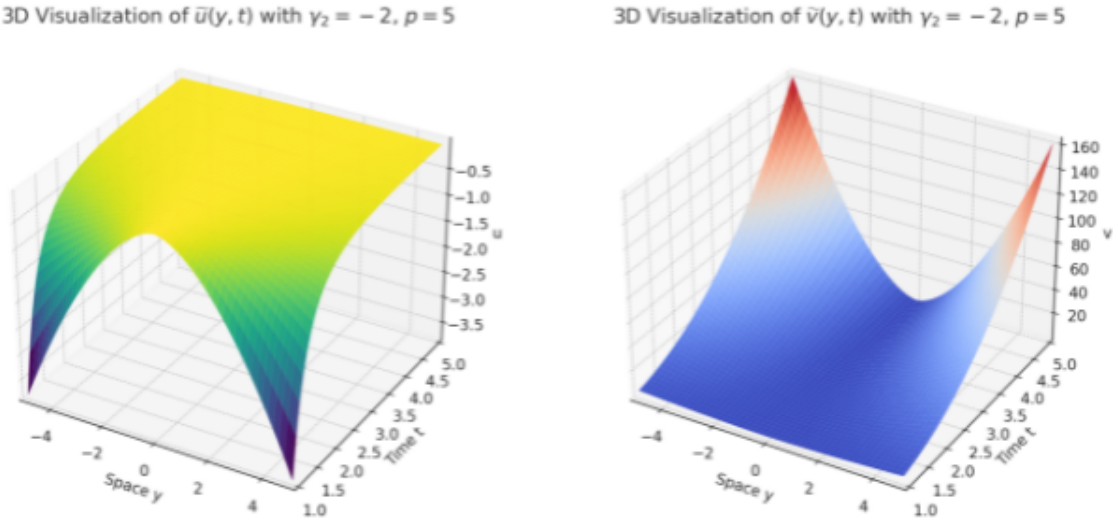

Figure 10. (**Left**): A 3D visualization of $\widetilde{u}(y,t)$ with the parameters $\gamma_2 = -2$ and $p = 5$. This plot illustrates how $\widetilde{u}$ evolves over the spatial domain from $-L$ to L and the time from 1 to 5. (**Right**): A 3D visualization of $\widetilde{v}(y,t)$ under the same parameters. The plot depicts the dynamics of $\widetilde{v}$, thereby highlighting its behavior over the adjusted time and space range. Both plots demonstrate the complex nature of the solutions and the impact of the parameter p on the flame dynamics, particularly with respect to a negative γ_2 value, thus providing deeper insights into the flame behavior in a variety of conditions. To obtain the pressure and temperature values, the reader is referred to the linear transformations in Equation (2) of [3].

The alteration in the value of p significantly impacts the rate at which the solutions, namely $\widetilde{u}(y,t)$ and $\widetilde{v}(y,t)$, evolve and disperse over time. This influence is a critical aspect in the realm of flame modeling, particularly as it pertains to how the flame's temperature and pressure profiles adapt to varying combustion conditions within porous media. In such

environments, the parameter p plays a pivotal role in characterizing the nature of diffusion and reaction processes. The value of p encapsulates the intricacies of heat and mass transfer within these media, thereby impacting how rapidly and efficiently flames spread. The choice of an appropriate p value is essential for accurately capturing the physicochemical interactions in porous media. It dictates the balance between diffusion-dominated and reaction-dominated regimes, which influences the overall flame structure. In practical scenarios, this could translate to varying flame behaviors, from slow, controlled combustion to rapid, intense burning depending on the porosity, permeability, and composition of the medium (refer to the linear transformations in Equation (1.2) of [3] to recover the pressure and temperature values that depend on the physical parameters). Accurately determining and applying the appropriate value of p is key to developing predictive models that can effectively describe and anticipate the behavior of flames in such complex environments. Experimental strategies to determine the parameter p typically involve controlled combustion tests within representative porous structures. These tests aim to analyze the flame's propagation speed, temperature distribution, and reaction kinetics under varying conditions. The setup might include a combination of high-speed imaging, thermocouples, and gas analyzers, which are used to capture the comprehensive data on flame dynamics.

7. Conclusions

In our study, we developed a model to explore the dynamic evolution of flames. This model utilizes the p-Laplacian operator for a more generalized diffusion representation, and it includes a bi-stable reaction term. We focused on the boundedness and uniqueness of solutions within weak formulations to ensure that our model's solutions were well defined and unique for general positive initial conditions. Our investigation also encompassed traveling wave solutions to provide a more intuitive understanding of flame dynamics. We employed the singular geometric perturbation theory to derive the analytical expressions for these traveling wave profiles. Numerical assessments were conducted to validate our theoretical predictions, particularly in determining an optimal traveling wave speed that aligns numerical results with analytical solutions. Furthermore, we examined self-similar structures within the flame propagation context, thereby providing solutions based on a scaling that can be of help for understanding the replication patterns in flame dynamics in line with the philosophy of similarity solutions. Looking ahead, an important future research direction would be to apply our model in laboratory experiments for real-world validation and data collection, which could provide refinements in the model. These adaptations, along with further numerical assessments being calibrated to lab conditions, may provide new ideas for our understanding and accuracy in simulating flame dynamics under various scenarios.

Author Contributions: Conceptualization, J.L.D.P.; Methodology, J.L.D.P.; Validation, J.L.D.P.; Formal analysis, S.u.R. and J.L.D.P.; Investigation, S.u.R. and J.L.D.P.; Resources, J.L.D.P.; Writing—original draft, S.u.R. and J.L.D.P.; Writing—review & editing, J.L.D.P.; Supervision, J.L.D.P. All authors have read and agreed to the published version of the manuscript.

Funding: This research received no external funding.

Institutional Review Board Statement: Not applicable.

Data Availability Statement: This work has no associated data nor materials.

Conflicts of Interest: The authors declare no conflicts of interest.

References

1. Gordon, P. Quenching and propagation of combustion fronts in porous media. *Commun. Math. Sci.* **2006**, *4*, 471–479. [CrossRef]
2. Gordon, P. Recent mathematical results on combustion in hydraulically resistant porous media. *Math. Model. Nat. Phenom. (MMNP)* **2007**, *2*, 56–76. [CrossRef]
3. Ghazaryan, A.; Gordon, P. KPP type flame fronts in porous media. *Nonlinearity* **2008**, *21*, 973. [CrossRef]

4. Murray, J.D. *Mathematical Biology*; Springer: Berlin/Heidelberg, Germany, 2003.
5. Shigesada, N.; Kawasaki, K. *Biological Invasions: Theory and Practice*; Oxford Series in Ecology and Evolution; Oxford UP: Oxford, UK, 1997.
6. IPCC. Climate change, synthesis report. In Proceedings of the IPCC Plenary XXVII, Valencia, Spain, 12–17 November 2007.
7. Kamal, M.M.; Mohamad, A.A. Combustion in porous media. *Proc. Inst. Mech. Eng. Part J. Power Energy* **2006**, *220*, 487–508. [CrossRef]
8. Viskanta, R. Combustion and heat transfer in inert porous media. In *Handbook of Porous Media*, 2nd ed.; CRC Press: Boca Raton, FL, USA, 2005; pp. 607–644.
9. Viskanta, R. Modeling of combustion in porous inert media. *Spec. Top. Rev. Porous Media Int. J.* **2011**, *2*, 181–204. [CrossRef]
10. Oliveira, A.A.M.; Kaviany, M. Nonequilibrium in the transport of heat and reactants in combustion in porous media. *Prog. Energy Combust. Sci.* **2001**, *27*, 523–545. [CrossRef]
11. Fisher, R.A. The wave of advance of advantageous genes. *Ann. Eugen.* **1937**, *7*, 355–369. [CrossRef]
12. Aronson, D.G.; Weinberger, H.F. Nonlinear diffusion in population genetics, combustion, and nerve pulse propagation. In *Partial Differential Equations and Related Topics: Ford Foundation Sponsored Program at Tulane University, January to May, 1974*; Springer: Berlin/Heidelberg, Germany, 2006; pp. 5–49.
13. Kanel, Y.I. On the stability of solutions of the cauchy problem for equations arising in the theory of combustion. *Mat. Sb.* **1962**, *59*, 245–288.
14. Roussier, V. Stability of radially symmetric travelling waves in reaction-diffusion equations. *Ann. L'Ihp Anal. Non Lineaire* **2004**, *21*, 341–379.
15. Kolmogorov, A.N.; Perrovsky, I.G.; Piskunov, N.S. A study of the equation of diffusion with increase in the quantity of matter, and its application to a biological problem. *Bull. Moskovsk. Gos. Univ.* **1937**, *1*, 1–26.
16. Schelkin, K.I. Influence of the tube walls roughness on the onset and propagation of detonation in gases. *Sov. J. Exp. Theor. Phys.* **1940**, *10*, 823–827.
17. Brailovsky, I.; Goldshtein, V.; Shreiber, I.; Sivashinsky, G. On combustion waves driven by diffusion of pressure. *Combust. Sci. Technol.* **1997**, *124*, 145–165. [CrossRef]
18. Billingham, J.; Needham, D.J. The development of travelling waves in quadratic and cubic autocatalysis with unequal diffusion rates: I. Permanent form travelling waves. *Phil. Trans. Phys. Sci. Eng.* **1991**, *334*, 1–24.
19. Kamin, S.; Vazquez, J.L. Fundamental Solutions and Asymptotic Behaviour for the p-Laplacian Equation. *Rev. Mat. Iberoam.* **1988**, *4*, 339–354. [CrossRef]
20. Bardi, M. Asymptotical spherical symmetry of the free boundary in degenerate diffusion equations. *Ann. Mat. Pura Appl.* **1987**, *148*, 117–130. [CrossRef]
21. Drabek, P. The p-Laplacian-mascot of nonlinear analysis. *Acta Math. Univ. Comenian.* **2007**, *76*, 85–98.
22. Lindqvist, P. *Notes on the p-Laplace Equation*; Department of Mathematics, Ohio State University: Columbus, OH, USA, 2006.
23. Oberman, A.M. Finite difference methods for the infinity laplace and p-laplace equations. *J. Comput. Appl. Math.* **2013**, *254*, 65–80. [CrossRef]
24. Benci, V.; d'Avenia, P.; Fortunato, D.; Pisani, L. Solitons in several space dimensions: Derrick's problem and infinitely many solutions. *Arch. Rational Mech. Anal.* **2000**, *15*, 297–324. [CrossRef]
25. Guo, Z.M.; Webb, J.R.L. Large and small solutions of a class of quasilinear elliptic eigenvalue problems. *Differ. Equ.* **2002**, *180*, 1–50. [CrossRef]
26. Lindqvist, P. On nonlinear Rayleigh quotients. *Potential Anal.* **1993**, *2*, 199–218. [CrossRef]
27. Smreker, O. Das Grundwasser und seine Verwendung zu Wasserversorgungen. *Zeitschr. Desvereines Dtsch. Ing.* **1879**, *23*, 347–362.
28. Smreker, O. Entwicklung eines Gesetzes für den Widerstand bei der Bewegung des Grund-wassers. *Zeitschr. Des Vereines Dtsch. Ing.* **1878**, *22*, 117–128.
29. de Pablo, A.; V-zquez, J.L. Travelling waves and fnite propagation in a reaction-diffusion Equation. *J. Difer Equ.* **1991**, *93*, 19–61. [CrossRef]
30. Fenichel, N. Persistence and smoothness of invariant manifolds for flows. *Indiana Univ. Math. J.* **1971**, *21*, 193–226. [CrossRef]
31. Akveld, M.E.; Hulshof, J. Travelling Wave Solutions of a Fourth-Order Semilinear Diffusion Equation. *Appl. Math. Lett.* **1998**, *11*, 115–120. [CrossRef]
32. Jones, C.K. *Geometric Singular Perturbation Theory in Dynamical Systems*; Springer: Berlin, Germany, 1995.
33. Enright, H.; Muir, P.H. *A Runge-Kutta Type Boundary Value ODE Solver with Defect Control*; Teh. Rep. 267/93; University of Toronto, Department of Computer Sciences: Toronto, ON, Canada, 1993.
34. Cobian-Iñiguez, J.; Aminfar, A.; Weise, D.R.; Princevac, M. On the Use of Semi-empirical Flame Models for Spreading Chaparral Crown Fire. *Front. Mech. Eng.* **2019**, *5*, 50. [CrossRef]